

Large-scale environment of $z \sim 5.7$ C IV absorption systems –II. Spectroscopy of Lyman- α emitters^{*}

C. Gonzalo Díaz^{1†}, Emma V. Ryan-Weber¹, Jeff Cooke¹, Yusei Koyama^{2,3},
and Masami Ouchi^{4,5}

¹Centre for Astrophysics and Supercomputing, Swinburne University of Technology, Hawthorn, VIC 3122, Australia

²National Astronomical Observatory of Japan, Mitaka, Tokyo 181-8588, Japan

³Institute of Space Astronomical Science, Japan Aerospace Exploration Agency, Sagami-hara, Kanagawa 252-5210, Japan

⁴Institute for Cosmic Ray Research, The University of Tokyo, Kashiwa, Chiba 277-8582, Japan

⁵Kavli Institute for the Physics and Mathematics of the Universe (WPI), The University of Tokyo, Kashiwa, Chiba 277-8583, Japan

Accepted. Received

ABSTRACT

The flow of baryons to and from a galaxy, which is fundamental for galaxy formation and evolution, can be studied with galaxy-metal absorption system pairs. Our search for galaxies around C IV absorption systems at $z \sim 5.7$ showed an excess of photometric Lyman- α emitter (LAE) candidates in the fields J1030+0524 and J1137+3549. Here we present spectroscopic follow-up of 33 LAEs in both fields. In the first field, three out of the five LAEs within $10h^{-1}$ projected comoving Mpc from the C IV system are within $\pm 500 \text{ km s}^{-1}$ from the absorption at $z_{\text{C IV}} = 5.7242 \pm 0.0001$. The closest candidate (LAE 103027+052419) is robustly confirmed at $212.8_{-0.4}^{+14} h^{-1}$ physical kpc from the C IV system. In the second field, the LAE sample is selected at a lower redshift ($\Delta z \sim 0.04$) than the C IV absorption system as a result of the filter transmission and, thus, do not trace its environment.

The observed properties of LAE 103027+052419 indicate that it is near the high-mass end of the LAE distribution, probably having a large H I column density and large-scale outflows. Therefore, our results suggest that the C IV system is likely produced by a star-forming galaxy which has been injecting metals into the intergalactic medium since $z > 6$. Thus, the C IV system is either produced by LAE 103027+052419, implying that outflows can enrich larger volumes at $z > 6$ than at $z \sim 3.5$, or an undetected dwarf galaxy. In either case, C IV systems like this one trace the ionized intergalactic medium at the end of cosmic hydrogen reionization and may trace the sources of the ionizing flux density.

Key words: early universe, galaxies: high redshift, galaxies: intergalactic medium, galaxies: distances and redshifts.

1 INTRODUCTION

The detection of metal absorption systems depends on the ionization balance of the absorbing gas, thus we can learn about the galaxies that reionized the Universe through the

study of the environment of metal absorption systems at the tail end of the epoch of reionization (EoR).

Statistical studies of C IV absorption systems across cosmic time (e.g. Ryan-Weber et al. 2009; Becker, Rauch & Sargent 2009; Simcoe et al. 2011; D’Odorico et al. 2013) suggest that some physical properties of the absorbing ‘clouds’, for example the size and the number density, are changing towards higher redshift. D’Odorico et al. (2013) compared the column densities of C IV, Si IV and C II in metal absorption systems across cosmic time and concluded that, at $z \sim 5.7$, C IV metal absorption systems trace less dense gas (overdensities $\delta \sim 10$) than at $z \sim 3$ ($\delta \sim 100$). In addition, Díaz et al. (2014, hereafter Paper I) report that two independent

^{*} Based on observations obtained at the W.M. Keck Observatory, which is operated as a scientific partnership among the California Institute of Technology, the University of California, and NASA, and was made possible by the generous financial support of the W.M. Keck Foundation.

[†] E-mail:gdiaz@swin.edu.au

lines of sight towards $z \sim 5.7$ C IV absorption systems are distant from the main projected over-densities of rest-frame UV bright Lyman break galaxy (LBG) candidates, opposite to the results at $z \sim 2-3$ (e.g. Adelberger et al. 2005; Steidel et al. 2010). Thus, it is possible that the absorbing gas at these two epochs is found in different environments on large-scales, which opens the possibility that the detection of C IV systems depends on properties that are linked to larger scales that go beyond the local density of the absorbing gas, such as the ionizing flux density background.

Interestingly, at scales of $10h^{-1}$ comoving Mpc, a projected over-density of Lyman- α emitter (LAE) candidates was found in the field J1030+0524 towards the C IV absorption system. Similarly in the field J1137+3549, the surface density of LAE candidates within $10h^{-1}$ comoving Mpc from the C IV system is higher than the average over the observed field of view of $\sim 80 \times 60h^{-1}$ comoving Mpc. If these over-densities of LAEs in the environment of C IV systems are confirmed (the aim of this paper), the association of highly ionized gas with a large scale excess of faint UV star-forming galaxies would be in agreement with the current literature where faint galaxies are found to dominate the ionizing photon budget at $z \sim 6$ (e.g. Cassata et al. 2011; Dressler et al. 2011; Finkelstein et al. 2012b; Ferrara & Loeb 2013; Cai et al. 2014; Fontanot et al. 2014). Moreover, it would imply that high ionization metal absorption systems at the end of the EoR can trace the highly ionized intergalactic medium (IGM).

At smaller scales, galaxy-metal absorption system pairs provide useful information on the distribution of metals. It has been observed that C IV absorption systems with column densities $N_{\text{CIV}} > 10^{14}$ at $z = 2-3$ are related to the circumgalactic medium (CGM) of LBGs (Adelberger et al. 2005; Steidel et al. 2010). Moreover, in these galaxies the red-shifted Ly α emission line and the blue-shifted interstellar absorption with respect to the systemic redshift determined by nebular emission lines (e.g. H α , H β and O III), is evidence for enriched gas moving at high velocities (hundreds of km s $^{-1}$). These galactic outflows are commonly observed in star-forming galaxies across cosmic time (Rupke, Veilleux & Sanders 2005; Weiner et al. 2009; Steidel et al. 2010; Coil et al. 2011; Jones, Stark & Ellis 2012; Bouché et al. 2012; Martin et al. 2012; Bradshaw et al. 2013; Karman et al. 2014) and represent an important source of chemical feedback widely explored in theoretical studies on the redistribution of metals from star-forming regions to the CGM and the IGM (Madau, Ferrara & Rees 2001; Oppenheimer & Davé 2006, 2008; Cen & Chisari 2011; Murray, Ménard & Thompson 2011; Tescari et al. 2011; Brook et al. 2012; Hopkins, Quataert & Murray 2012; Shen et al. 2012; Pallottini et al. 2014).

Although it is well accepted that star-forming galaxies can produce outflows that will enrich their CGM and potentially the IGM, the abundance of metal absorption systems and the sizes of the enriched regions suggest that a significant fraction of the metals observed in the CGM and IGM at redshift $z = 1.7-4.5$ have been produced by satellites and progenitors of the observed galaxies during an early stage of galaxy formation at redshifts above 6 (e.g. Porciani & Madau 2005; Martin et al. 2010). This is commonly known as pre-galactic enrichment. For example, Shen et al. (2012) use a detailed cosmological hydrodynamic simulation to study

the sources of metals in the CGM of a $z = 3$ LBG, and find that metals observed at low radii ($< 3R_{\text{vir}}$) are mainly produced in the host galaxy while metals at larger radii ($> 3R_{\text{vir}}$) are mainly produced in the satellite companions. Moreover, the metals observed at $> 2R_{\text{vir}}$ were released at redshift $z > 5$. Therefore, searching for star-forming galaxies close to the highest redshift C IV absorption systems known to date is the next step in testing theories on the enrichment of the IGM.

This work presents the spectroscopic observations obtained with DEIMOS on Keck-II for the LAE photometric candidates in Paper I. The follow-up spectroscopy demonstrates that the $z \sim 5.7$ LAE selection criteria is robust, in particular for bright sources in the narrow-band filter NBC IV. We report tentative evidence that the projected over-density of LAEs in the field J1030+0524 corresponds to an excess of sources within ± 500 km s $^{-1}$ from the second C IV absorption system at $z \gtrsim 5.5$ in the line of sight to the QSO ($z_{\text{CIV,b}} = 5.7242 \pm 0.0001$). However, better data is needed for at least two of the sources, to confirm the nature of emission line currently detected with very low signal-to-noise. In the field J1137+3549, the sample of LAEs is not at the redshift of the C IV system and therefore does not trace the environment of this absorption system.

Our spectroscopic campaign confirmed the redshift of LAE 103027+052419 whose angular separation on the sky implies a distance of $212.8_{-0.4}^{+14} h^{-1}$ physical kpc from the absorption system C IV $_b$, mentioned above. This is evidence that the strongest C IV system known at $z \gtrsim 5.5$ is associated with a detectable star-forming galaxy. Considering the evidence of the high incidence of galactic outflows at high redshift (e.g. Vanzella et al. 2009; Steidel et al. 2010; Jones, Stark & Ellis 2012; Shibuya et al. 2014), it is very likely that LAE 103027+052419 hosts some kind of outflow. Therefore, the question of interest is whether or not the carbon produced by an earlier generation of stars in the LAE could have reached the distances at which the C IV absorption system is observed.

The analysis shows that the impact parameter of $212.8h^{-1}$ physical kpc is difficult to reconcile with a typical galactic wind scenario due to the short time since the Big Bang at which the LAE-C IV system pair is observed. As a result, even if the metals were distributed by an outflow from the LAE, the mechanisms should have already been in place at a time that is consistent with the pre-galactic enrichment scenario. Moreover, it is possible that the metals in the absorbing gas were born in undetected dwarf galaxies that polluted the IGM, while the LAE only provides the ionizing radiation to maintain the triply ionized carbon. Therefore, the simplest explanation for our results is that LAE 103027+052419 is associated with the C IV system as the source of ionizing radiation instead of the source of enrichment. The main implication is that C IV absorption systems at $z \sim 5.7$ trace highly ionized IGM. This is in agreement with predictions from cosmological simulations (e.g. Oppenheimer, Davé & Finlator 2009) and suggests that C IV systems in the post-reionization Universe are important sources of information about the ionization state of the IGM.

This paper is organised as follows: Section 2 describes the observations, Section 3 presents the spectroscopic catalogue of LAEs and reviews the contamination in the sample, Section 4 reviews the colours and magnitudes of $z \sim 5.7$

LAEs, Section 5 presents the redshift distribution of the sample and Section 6 discusses the distribution of LAEs in the environment of C IV absorption systems, both projected and in the line of sight. After that, a description of the LAE-C IV system pair in the J1030+0524 field is presented in Section 7. Then, the rest-frame equivalent width of the Ly α line (hereafter EW₀) and the velocity shift of the Ly α maximum (hereafter Δv_{MAX}) are presented in Sections 8 and 9, respectively. Finally, the origin of the C IV system in the field J1030+0524 is discussed in Section 10 and the conclusions are summarised in Section 11. Throughout this work we use AB magnitudes and assume a flat universe with $H_0 = 70 \text{ km s}^{-1} \text{ Mpc}^{-1}$, $\Omega_m = 0.3$ and $\Omega_\Lambda = 0.7$.

2 OBSERVATIONS AND DATA REDUCTION: DEIMOS, KECK TELESCOPE

This work is based on the spectroscopic observations of $z \sim 5.7$ LAE photometric candidates from Paper I. The fields of view are centred on QSOs SDSS J103027.01+052455.0 ($z_{\text{em}} = 6.309$, RA = $10^{\text{h}}30^{\text{m}}27^{\text{s}}.01$, Dec. = $05^{\circ}24'55''.0$) and SDSS J113717.73+354956.9 ($z_{\text{em}} = 6.01$, RA = $11^{\text{h}}37^{\text{m}}17^{\text{s}}.73$, Dec. = $35^{\circ}49'56''.9$) (Fan et al. 2006), hereafter J1030+0524 and J1137+3549. This section describes two data sets obtained with the DEIMOS spectrograph on the Keck-II telescope: first, the main data set collected the nights of the 27th and 28th of February 2012¹, and second, additional data obtained at the end of the night of the 26th of February 2014².

For the observing run of 2012, the seeing was in the range 0.55–0.8 arcsec FWHM during the first night and 0.55–1.0 arcsec FWHM during the second night. In order to acquire spectra of high redshift galaxies and to enable the identification of many key features of low redshift contaminants, we used the OG550 order-blocking filter and the 830 line mm^{-1} grating (830G), which provides wavelength coverage from ~ 6500 to $\sim 10000 \text{ \AA}$ with a central wavelength $\lambda_c = 8579 \text{ \AA}$. For a 1 arcsec slit width, the spectral resolution is $\text{FWHM} = 2.5 \text{ \AA}$ (or 91.4 km s^{-1} at 8200 \AA), which is sampled with a scale of 0.47 \AA per pixel. The 830G grating provides sufficient resolution to identify the O II emission doublet of galaxies at $z \sim 1.19$ ($\lambda_{\text{obs}} \sim 8166 \text{ \AA}$), which are the main contaminants in $z \sim 5.7$ LAE samples.

In each of the two fields, three multi-slit masks were used, carefully designed with position angles that minimise the flux lost due to atmospheric dispersion. Single exposure times of 1200 seconds were adopted for all the exposures but the number of exposures per mask varied due to priority and weather conditions. In particular, for the field J1030+0524 the number of exposures (and total exposure time) per mask was 14 (16800 s), 7 (8400 s) and 3 (3600 s). For the field J1137+3549, we acquired 12 (14400 s), 9 (10800 s) and 3 (3600 s) exposures per mask. Therefore, the exposure time is not uniform across the LAE sample.

One additional mask per field was observed in February 2014 with the same instrument but lower spectral resolution and lower signal-to-noise ratio (S/N). We used the 600 line

mm^{-1} grating (600ZD) and the GG495 order-blocking filter covering the wavelength range ~ 5000 to $\sim 10500 \text{ \AA}$ with a scale of 0.65 \AA per pixel. The width of the slits was 1 arcsec resulting in a $\text{FWHM} = 3.5 \text{ \AA}$ (128.0 km s^{-1} at 8200 \AA). For the field J1030+0524, only two exposures of 800 seconds each were obtained, which provided the detection of an emission line in three LAE candidates, although with low significance. Unfortunately, the S/N is not sufficient to distinguish lower redshift contamination because companion emission lines would be undetected and the symmetry of the line cannot be determined with sufficient accuracy (see Section 3.2). Thus, the data from February 2014 for the field J1030+0524 is presented as ‘tentative identification’ and are included in the analysis with a note of caution that the spectroscopic detections cannot robustly confirm nor rule-out the high-redshift nature of the sources. In the field J1137+3549, three exposures of 1500 seconds (4500 s) were obtained and provided sufficient S/N to measure the redshift of LAEs and to identify contaminants. Thus, the additional data on this field are included in our analysis together with the main data set.

Most of the reduction process was performed in IDL using the DEIMOS pipeline software in the SPEC2D package (Cooper et al. 2012; Newman et al. 2013). The pipeline processes the flats and arcs, which are rectified into rectangular arrays, and calculates the wavelength solution of the 2D data array. Then, it applies corrections for flatfield and fringing to the science data of each slit, which are also rectified into rectangular arrays. A b-spline model of the sky is obtained for each of the individual science exposures, and subtracted from them. The residuals are then combined into an inverse variance weighted average 2D spectrum of each slit and cosmic-rays rejection is applied on individual pixels.

The SPEC2D package does a good job, in most cases, in the spatial direction along the slit which allows for a correct curvature rectification. However, in the dispersion direction, the 2D output spectra shows a wavelength shift in different directions respect with each other. This effect is obvious in Figure 1 that shows a section of an image created by the SPEC2D pipeline for quality inspection (‘All-slits0.[name_of_the_mask].fits’), just before the 1D spectra are extracted. The solid line rectangle highlights the sky residuals of two consecutive slits which are not aligned. In order to solve this problem, a new wavelength dispersion solution for each 1D object spectrum was obtained, using the spectrum of the sky as comparison spectrum.

Standard IRAF tasks (e.g. IDENTIFY, REFSPECTRA and DISPCOR) and the high-resolution spectral atlas of night-sky emission lines from Osterbrock et al. (1996) as reference were used to calculate the correct wavelength dispersion solution and to apply it to the objects spectra. This procedure was applied to the main data set only since the wavelength dispersion of the additional lower resolution data is properly calculated by SPEC2D. First, the 1D spectrum of each object was boxcar extracted from the 2D spectrum output of SPEC2D by direct sum of the counts in pixels with constant wavelength. The variance was obtained as the direct sum of the variances (i.e. errors added in quadrature). The extraction box position was defined by visual inspection to include all the pixels that showed flux in the 2D spectrum at the position of the object. Secondly, the spectrum of the sky was extracted from the same slit and position as the object be-

¹ Program ID: W136D

² Program ID: N121D

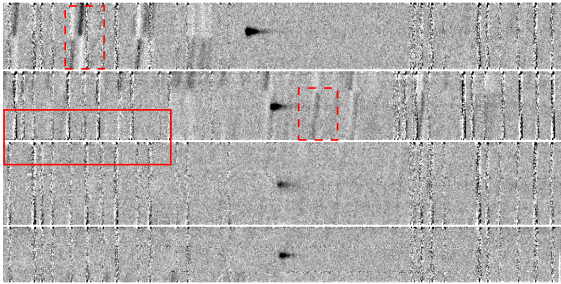


Figure 1. Example of a control image from SPEC2D (‘All-slits0.xxxx.fits’) showing four consecutive slits. The image is created to check the reduction process before the 1D spectrum extraction. Two major problems can be identified. First, red dashed line rectangles show sky emission probably from other slits. The reflected light is not removed by the model of the background and produces undesired residuals in all the slits. Second, the red solid line rectangle shows that the skylines residuals of consecutive slits are not aligned, which indicates that the automatic wavelength calibration does a poor job with our data. These effects can be avoided with an additional 5° tilt to the position angle of the slits.

fore the b-spline model of the background sky was removed from the data spectrum. Thirdly, we obtained a wavelength dispersion solution for the sky emission lines measured in the same CCD columns as the object (pixel columns in DEIMOS data correspond to the dispersion direction). The typical RMS of the fit is $\sim 0.03\text{--}0.05 \text{ \AA}$. Finally, the same wavelength solution was assigned to the object spectrum. The output of this process is the reduced 1D spectra of the 33 line emitters presented in the following section.

3 SPECTROSCOPIC CATALOGUE OF $z \sim 5.7$ LAES

This section presents the spectroscopic sample and summarises the possible sources of contamination. First, we present the data. Second, we comment on the contamination level and the approach adopted to remove contaminant sources. Third, we search for evidence of Active Galactic Nuclei (AGN) among the objects in the sample.

The complete sample contains 33 spectra of which 28 are photometric LAE candidates and five are extra detections that were not photometrically selected due to insufficient signal-to-noise in the NBC IV band ($S/N_{\text{NBC IV}} \lesssim 5$). Spectroscopic quantities and other estimates based on the spectroscopic redshift of each LAE are presented in Tables A1, A2, A3 and A4 in Appendix A. Contamination was determined based on the asymmetry of the emission lines and visual inspection of the spectra. The contamination level in the photometric sample is $\sim 10\text{--}20$ per cent, based on 25 LAE candidates with reliable spectroscopy (i.e. excluding the three low resolution spectra in J1030+0524). Finally, no evidence of AGN (e.g. emission from N V(1241 \AA), Si IV+O VI](1400 \AA) and N IV(1483,1487 \AA) was found in the sample. However, the search is limited by the lack of information on other wavelengths (e.g.: X-rays, sub-mm, etc.) and the high contamination of skylines in the observed wavelength range.

3.1 The sample

In the J1030+0524 field, spectra of 17 photometric LAE candidates have been obtained. Three of the LAEs were observed using the 600ZD grating and short exposure times, thus the asymmetry of their emission line cannot be measured with sufficient precision. We opted not to include these three objects in our discussion but, for completeness, we do measure the position of the emission line and comment on them when we consider it relevant. This leaves us with 14 photometric candidates with reliable spectroscopy. In addition, four objects with $S/N_{\text{NBC IV}} \lesssim 5$ were spectroscopically confirmed to have an emission line and were included in the analysis. Thus, the total sample contains 21 spectra of which 18 (14+4) have sufficient S/N for a fair assessment of the asymmetry of the line, while the three low resolution spectra are only used to measure the position of the line. The sample is presented in Figure 2, which shows the spectra and photometry snapshots on the four bands R_c , i' , NBC IV and z' , used in the photometric selection of Paper I.

In the field J1137+3549, we acquired spectra of 11 photometric LAE candidates. Four of them were observed using the 600ZD grating with exposure times long enough to provide good quality spectroscopy to determine the asymmetry of the emission line. Thus, we include the low-resolution data of this field in our discussion. One additional object with $S/N_{\text{NBC IV}} \lesssim 5$ was included in the analysis after the spectroscopic confirmation of an emission line. Hence, the sample in this field contains 12 spectra (11+1) which are presented in Figure 3.

The objects in both Figures 2 and 3 are sorted according to the asymmetry of the emission line, decreasing from top to bottom. The ID numbers on the left hand side are for reference to Tables A1–A4 (Appendix A), which present the information on each of the candidates. Spectra obtained with the 600ZD grating are labeled as such. All the other spectra were obtained with the 830G grating. Additional objects with $S/N_{\text{NBC IV}} \lesssim 5$ (i.e. not in the sample of photometric LAE candidates) are also indicated with the corresponding label. The ‘X’ symbol indicates if the object does not meet the asymmetry condition for $z \sim 5.7$ LAE (see Section 3.2.1) The next section presents the search for contamination from foreground sources in the sample of LAEs.

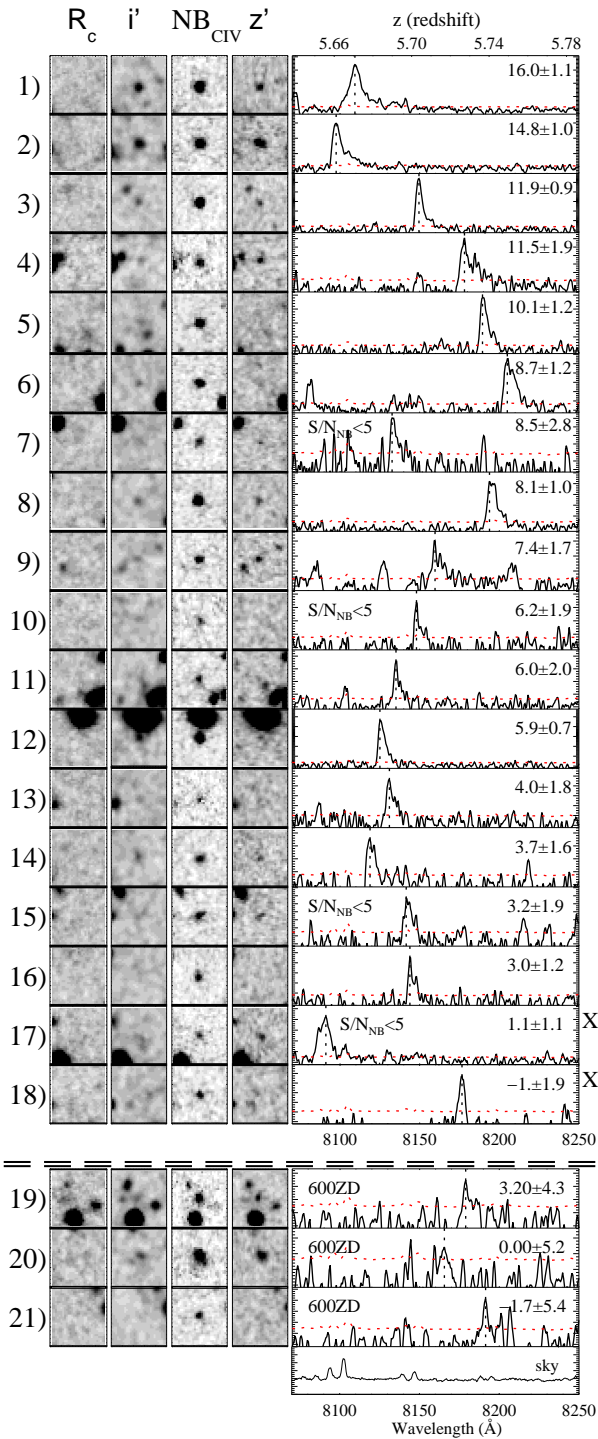


Figure 2. Snapshots and spectra of the $z \sim 5.7$ LAEs in the field J1030+0524. Images on the left correspond to R_c , i' , NB_{CIV} and z' bands, the snapshot boxes are 6×6 arcsec. In the spectra, the vertical scale is arbitrary, the peak of the emission lines are indicated with vertical dotted lines, and the 1σ error spectra are plotted with red dotted lines. The objects are arranged by decreasing weighted skewness $S_{w,10\%}$ (defined in Section 3.2.1) which is given in the top-right corner of each spectrum. The 'X' indicates objects with $S_{w,10\%} < 3.0$ and the bottom panel shows the sky spectrum. The 600ZD spectra are below the double-dashed line and do not have the sensitivity required for our analysis. Nevertheless, emission lines are detected in the three cases, hence we present the data for completeness.

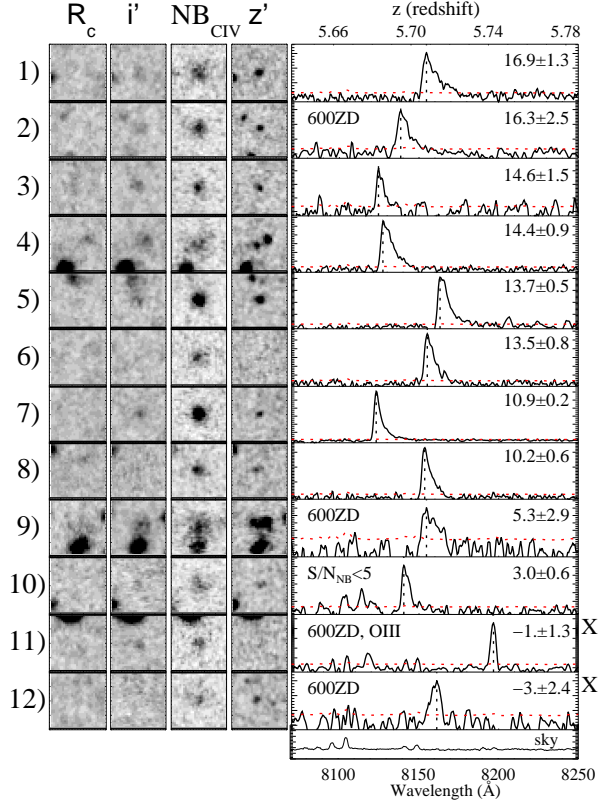


Figure 3. Snapshots and spectra of the $z \sim 5.7$ LAEs in the field J1137+3549. Similar to Figure 2, images in the left hand correspond to 6×6 arcsec snapshot boxes of R_c , i' , NB_{CIV} and z' bands, and the objects are arranged by decreasing weighted skewness $S_{w,10\%}$. Spectra obtained with the 600ZD grating are labeled. The confirmed O III emitter is ranked #11.

3.2 Contamination in the spectroscopic sample

Photometric LAE candidates are selected based on an excess of flux in the NBC IV filter. This excess could result not only from Ly α at $z \sim 5.7$ but also from O II ($\lambda 3726, 3729 \text{ \AA}$) at $z \sim 1.17\text{--}1.20$, O III ($\lambda 5007 \text{ \AA}$) at $z \sim 0.61\text{--}0.64$ and H α ($\lambda 6563 \text{ \AA}$) at $z \sim 0.23\text{--}0.25$. Lower redshift contaminants are removed by a broad band colour condition (e.g. $(R_c - z') > 1.3$, Paper I) that aims to identify the flux decrement produced at $\lambda_{\text{rest}} \lesssim 1216 \text{ \AA}$ and $\lambda_{\text{rest}} \lesssim 912 \text{ \AA}$ by the absorbing neutral hydrogen in the Universe at $z \sim 5.7$. However, some contamination remains, in particular among fainter emitters.

This section presents the criteria adopted to remove lower redshift contaminants based on two observational characteristics of $z \sim 5.7$ LAEs. First, the Ly α line at this redshift is asymmetric due to neutral hydrogen in the galaxy, the CGM and IGM close to the source (Zheng et al. 2010) whilst the emission line from a lower redshift contaminant is typically symmetric (e.g. O III and H α), or a doublet (e.g. O II). Secondly, if the emission is Ly α , there are no other nebular emission lines in the observed wavelength window. The presence of additional UV emission lines in a $z \sim 5.7$ LAE is typically associated with an AGN. Because AGNs produce well identified emission lines such as N V, Si IV+O VI], N IV and C IV, the sole detection of any of these transitions would indicate an AGN. However, the fraction of AGNs among $z \sim 5.7$ LAEs is negligible (e.g. Ouchi et al. 2010). Hence, the most common cases present no emission lines other than Ly α . As a result, lower redshift contaminants can be spectroscopically identified from the presence of additional emission lines and/or from the shape (asymmetry) of the emission line.

3.2.1 Weighted skewness

The Ly α emission in our sample of LAEs is affected by the neutral hydrogen content of the post-reionization Universe. The number of intervening neutral hydrogen (H I) systems increases to higher redshifts (e.g. Becker et al. 2013). As a result, the net effect in the Ly α emission line is a complete absorption of the blue side. This asymmetry could be enhanced by Ly α photons emitted from the galaxy in a direction opposite to the observer, which are scattered back towards the Earth after interacting with the receding side of a galactic wind (e.g. Hansen & Oh 2006; Verhamme et al. 2006; Dijkstra & Wyithe 2010; Verhamme et al. 2014). Therefore, these photons are doppler shifted according to the speed of the wind and, by the time they reach the neutral IGM towards the observer, they have been redshifted and cannot be absorbed by the intervening neutral hydrogen. The result is a typical red ‘tail’ that in the 2D spectrum can be seen like a ‘tadpole’ as in the four examples of Figure 1. For this reason, the asymmetry of the high redshift Ly α emission has become the main discriminant for lower redshift interlopers (e.g. Rhoads et al. 2003; Kashikawa et al. 2006; Shimasaku et al. 2006; Kashikawa et al. 2011).

In this work, we adopted the weighted skewness criteria proposed by Kashikawa et al. (2006) to quantify the asymmetry of the line profile. We estimate the weighted skewness $S_{w,10\%}$ using $\lambda_{10\%,R}$ and $\lambda_{10\%,B}$ which are the wavelengths

where the flux from the emission drops to 10 per cent of the peak value on the red and blue sides, respectively.

In particular, from the 18 spectroscopic detections in the field J1030+0524, we find 16 with a skewness $S_{w,10\%} \geq 3.0$ which are considered LAEs and two with $S_{w,10\%} < 3.0$ which are considered contaminants. In the field J1137+3549, 10 emission lines have $S_{w,10\%} \geq 3.0$ and two have $S_{w,10\%} < 3.0$, of which one is confirmed to be O III ($\lambda 5007$) by the detection of O III ($\lambda 4959$).

Regarding the photometric sample (i.e. not including the $S/N_{\text{NBC IV}} \lesssim 5$ objects), we report that 13 out of 14 photometric LAE candidates (~ 93 per cent) and 9 out of 11 photometric LAE candidates (~ 82 per cent) are spectroscopically confirmed LAEs in the fields J1030+0524 and J1137+3549, respectively. These translates to a contamination fraction in the photometric sample of $\sim 10\text{--}20$ per cent. Interestingly, the objects in both fields that do not satisfy the asymmetry criteria are among the fainter emitters. Finally, we note that the asymmetry criterion as a discriminant of lower redshift emitters is supported by the skewness measurement of an O II emitter and an O III emitter in our data.

3.2.2 The O II doublet

Among the possible contamination, the main sources are O II emitters at $z \sim 1.17\text{--}1.2$ because the Balmer break could mimic the Ly α forest decrement at $z \sim 5.7$. Fortunately, the O II doublet has a wavelength separation of $2.8 \text{ \AA} \times (1+z)$, which is $\sim 6.1 \text{ \AA}$ at $z \sim 1.18$. Thus, the instrument configuration used in our observations provides the spectral resolution to identify the O II doublet if detected with sufficient S/N. For example, Figure 4 shows the 2D and 1D spectrum of a O II emitter detected in the field J1137+3549 but not a photometric LAE candidate. The 1D spectrum has been smoothed with a three pixel size boxcar and the O II doublet is clearly distinguishable. The maximum of each line was measured at $\lambda_{3727.092} = 8167.56 \text{ \AA}$ and $\lambda_{3729.875} = 8174.05 \text{ \AA}$ which correspond to $z = 1.1914 \pm 0.0001$. The skewness of the doublet is $S_{w,10\%} = -3.7 \pm 0.9$ which indicates that the asymmetry is opposite to that of the Ly α line: the red emission line $\lambda 3729.875$ is brighter than the blue emission line $\lambda 3727.092$. Therefore, the asymmetry of the doublet is easily detected with the resolution of our observations and we are able to discriminate O II from Ly α .

3.2.3 Additional emission lines

Detection of nebular emission lines provides a robust identification of lower redshift galaxies. The spectral range covered by the data allowed us to search for other emission lines associated with O II emitters and O III ($\lambda 5007 \text{ \AA}$) emitters. In the first case, we looked for Ne III, H δ and H γ at the corresponding wavelengths, as shown in Figure 5 (top panel). In the second case, we searched for the presence of O III ($\lambda 4959 \text{ \AA}$), H β , H γ and H δ , in the wavelength windows highlighted in the middle panel of Figure 5. A careful inspection of the 2D and 1D spectra resulted in the detection of an O III emitter in the spectroscopic sample of LAE candidates in the field J1137+3549.

The object is labeled ‘O III’ in Figure 3, and is shown in

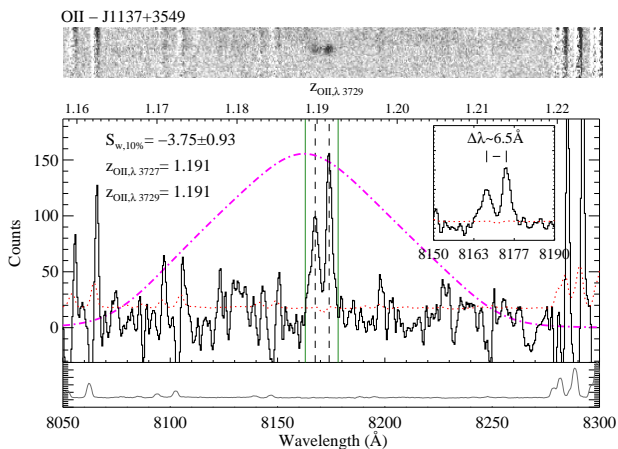


Figure 4. Example of an O II emitter at $z_{\text{O II}} = 1.191$ observed with the 830G grating. The observed wavelength of the O II doublet is in the range covered by the NBC IV filter and, therefore, is an example of a possible source of contamination. *Top*: Snapshot of the 2D slit spectrum in the wavelength range covered by the NBC IV filter. *Middle*: 1D spectrum smoothed over 3 pixels and close-up of the emission line. The doublet is clearly resolved and the continuum is below the 1σ error (red dotted line). The magenta dot-dashed line is the scaled transmission curve of the NBC IV filter. The green vertical lines enclose the wavelength range used to determine the skewness. *Bottom*: Sky spectrum for reference.

better detail in Figure 6. The O III ($\lambda 4959 \text{ \AA}$) emission line is seen at $\lambda = 8117.57 \text{ \AA}$. No other emission lines were detected. Moreover, the weighted skewness of the brightest emission line ($\lambda_{\text{rest}} = 5007 \text{ \AA}$) is $S_{w,10\%} = -1.7 \pm 1.0$ which validates the asymmetry criterion.

Although the 830 line mm^{-1} grating provides wavelength coverage from 6500 to 10000 \AA , the effective wavelength range observed in each slit depends on its position on the mask. Therefore, not all the spectra cover the wavelength range necessary to explore the presence of all the possible additional emission lines that would reveal the low-redshift nature of an object. Moreover, many of the possible additional emission lines that would confirm a low redshift interloper are buried in a forest of sky-lines residuals, which makes them more difficult to be detected (Figure 5). This problem is more severe for faint objects detected with low S/N.

Finally, if the emission in the NBC IV filter was H α , the wavelength coverage of the data does not reach the wavelength of the nearest strong emission lines like H β and O III (Figure 5, bottom panel). Therefore, H α cannot be identified by the presence of other emission lines. As a result, because H α is symmetric, identification of H α emitters at $z \sim 0.23$ – 0.25 relies mainly on the symmetry of the line. However, the spectral energy distribution is also a discriminant if continuum is detected because, for example, an H α emitter would show continuum flux at both sides of the emission line.

In summary, the abundant emission from the night sky reduces our ability to detect additional emission lines in the galaxies’ spectra. The O II emitter in Figure 4 and the LAE candidate that shows clear evidence for additional emission lines (Figure 6) also have negative asymmetry line profiles. Therefore, these objects support the asymmetry criterion

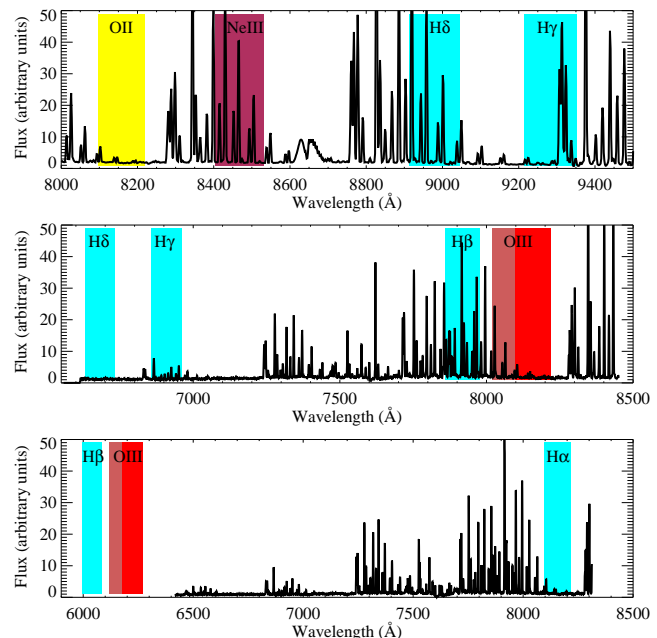


Figure 5. Expected wavelength of emission lines typically present in lower redshift star-forming galaxies that could be observed if the emission in the NBC IV is either O II, O III or H α . The sky spectrum is shown for reference. Many of the additional lines are buried in sky emission lines which reduces our ability to identify them. *Top*: O II emitters at $z = 1.17$ – 1.20 . The wavelength intervals of emission lines that, within the observed spectral range, are commonly associated with O II ($\lambda 3726, 3729 \text{ \AA}$) are labeled in the plot: Ne III, H δ and H γ . *Middle*: O III emitters at $z = 0.61$ – 0.64 . In this case, the associated emission lines that could be observed are O III ($\lambda 4959 \text{ \AA}$), H β , H γ and H δ . *Bottom*: H α at $z = 0.23$ – 0.25 . The spectral range of the data does not sample the next brighter lines after H α (i.e.: O III and H β).

adopted in this work to discriminate lower redshift contaminants in the LAE sample. We conclude that additional emission would confirm the low redshift nature of an object but cannot be the only criterion used to detect contamination in the sample.

3.2.4 Magnitude dependant contamination fraction

Among fainter emitters, low S/N reduces the ability to resolve a doublet from a single line and to accurately measure the asymmetry of the emission. Therefore, the level of contamination is expected to increase towards fainter magnitudes. The data set used in this work seems to agree with this expectation since, first, sources brighter than NBC IV = 24.7 mag are confirmed LAEs ($S_{w,10\%} \geq 3$) and, second, LAE candidates with $S_{w,10\%} < 3$ are fainter than NBC IV = 24.7 mag.

Figure 7 shows the relation between $S_{w,10\%}$ and two photometric quantities: NBC IV magnitude and the flux excess in NBC IV measured by the colour ($i' - \text{NBC IV}$). Blue and red circles are LAEs in the fields J1030+0524 and J1137+3549, respectively, observed with the 830G grating. Objects observed with the 600ZD grating in the later field are represented by red squares. We do not consider observations of J1030+0524 obtained with this grating be-

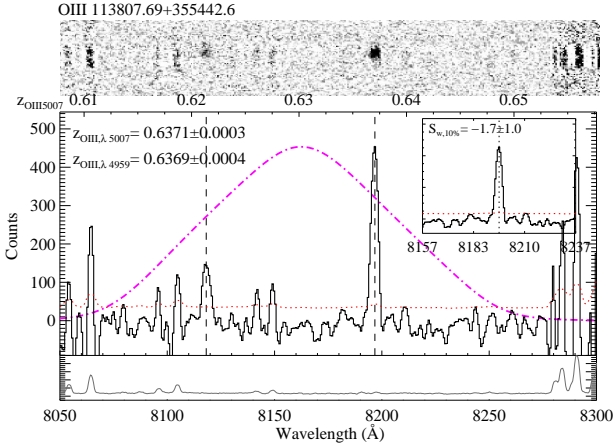


Figure 6. O III emitter in the photometric sample of LAE candidates observed with the 600ZD grating. Two emission lines are clearly detected and correspond to O III($\lambda 5007 \text{ \AA}$) and O III($\lambda 4959 \text{ \AA}$) at $z_{\text{O III}} \sim 0.637$. *Top*: Snapshot of the 2D slit spectrum in the wavelength range covered by the NBC IV filter. *Middle*: 1D spectrum smoothed over 3 pixels and close-up of the emission line at $\lambda_{\text{rest}} = 5007 \text{ \AA}$, which has a skewness < 3 . The red dotted line is the 1σ error and the magenta dot-dashed line is the scaled transmission curve of the NBC IV filter. *Bottom*: Example of sky spectrum for reference.

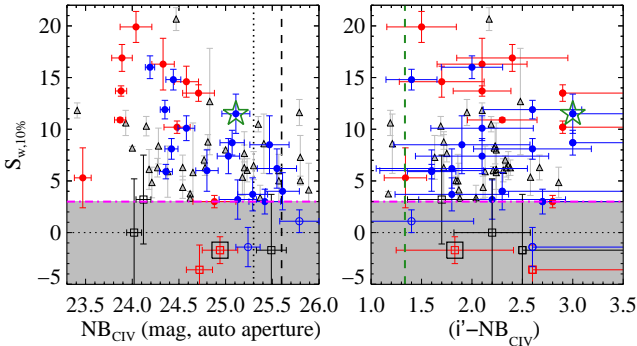


Figure 7. Weighted skewness as a function of NBC IV magnitude and $(i' - \text{NBC IV})$ colour. Blue and red circles correspond to the fields J1030+0524 and J1137+3549, respectively. The star symbol highlights LAE 103027+052419 (see Section 7). Triangles are SDF LAEs (Shimasaku et al. 2006). Open squares correspond to low resolution data obtained with the 600ZD grating in the field J1030+0524, which are presented only for completeness. The dot-dashed horizontal line is the boundary $S_{w,1\sigma} = 3$ above which objects are considered LAEs (solid symbol). *Left*: NBC IV magnitude versus $S_{w,10\%}$. Brighter objects tend to have higher $S_{w,10\%}$. In particular, spectroscopic LAEs with NBC IV < 24.7 have $S_{w,10\%} \geq 3.0$. The two vertical lines indicate the 5σ limit magnitude in the field J1030+0524 (dashed line) and the field J1137+3549 (dotted line). *Right*: $(i' - \text{NBC IV})$ versus $S_{w,10\%}$. In this case, there is not clear correlation between the two quantities. The vertical dashed line shows the condition $(i' - \text{NBC IV}) > 1.335$ used in the photometric selection criteria for LAEs in Paper I.

cause the lower S/N results in skewness measurements with large errors, but for completeness we show them in the plot with black open squares. The star symbol indicates LAE 103027+052419 at $z = 5.724$, which is the closest LAE

to the CIV absorption system at $z_{\text{CIV,b}} = 5.7242$ in the field J1030+0524 (see Section 7). Points above and below $S_{w,10\%} = 3$ (grey area) are represented by solid and open symbols, respectively. In the left panel, we note a trend for fainter objects to have lower skewness, with objects in both fields following the same tendency. In comparison, however, the spectroscopic sample of $z \sim 5.7$ LAEs in the Subaru Deep Field (SDF, Shimasaku et al. 2006), over-plotted with grey triangles in Figure 7, seems more uniformly scattered across the range of magnitudes. The spectroscopic sample of SDF LAEs includes data with different resolution (FWHM=9.5, 7.1 and 3.97 \AA). Moreover, the spectral resolution of the data affects the ability to measure the line skewness, and is therefore a source of systematic error when comparing data with different resolutions, like in Figure 7. As a result, we need larger and homogeneous samples to explore the morphology of the high-redshift Ly α emission and the information behind it in a consistent way.

Finally, no obvious correlation is seen between $S_{w,10\%}$ and $(i' - \text{NBC IV})$, which are plotted in the right panel of Figure 7. Objects above the grey area ($S_{w,10\%} \geq 3$) show significant scatter in $(i' - \text{NBC IV})$. This is observed in our sample and SDF LAEs, and means that robust and bright spectroscopically confirmed LAEs can show small or large narrow-band flux excess, regardless of the asymmetry of the line. Below $S_{w,10\%} = 3$, photometric candidates can also drop-out of the i' -band and reach $(i' - \text{NBC IV}) > 2.5$, in which case the colour $(i' - \text{NBC IV})$ is only a lower limit and is more than a magnitude greater than the condition $(i' - \text{NBC IV}) > 1.335$ in the photometric selection criteria for LAEs of Paper I. We conclude that the current data cannot robustly confirm nor rule out the existence of a correlation between the measured asymmetry of the emission line and the narrow-band photometric properties of the source. Nevertheless, we recall that contaminants are fainter than NBC IV = 24.7 mag which is not enough to claim a correlation, but is useful to keep in mind in further analysis of the sample.

3.3 Active Galactic Nuclei in the $z \sim 5.7$ LAE sample

The Ly α emission can also be powered by an AGN. However, AGNs are rarely found among high redshift LAEs (e.g. Wang et al. 2004; Ouchi et al. 2008; Zheng et al. 2010). Unfortunately, we do not have information from other wavelengths (e.g. radio, X-ray, infrared, submillimeter) nor we have information on the rest-frame optical emission lines to search for AGN activity in the $z \sim 5.7$ LAE sample. Therefore, we can only explore the presence of AGNs by searching for high ionization UV emission lines produced by AGN activity. However, the wavelength range of our data does not cover the typically strong CIV emission, thus we only searched for N V, Si IV+O VI] and N IV. Moreover, N V and Si IV+O VI], which are the brighter emission lines that could have been detected in the spectral range of the data, would be in regions of the spectrum that are heavily affected by sky emission lines. This is clearly seen in Figure 8. As a result, our ability to identify AGNs is very limited. Nevertheless, after careful visual inspection of each 2D and 1D spectra, we report no evidence of AGN activity in the spectroscopic sample.

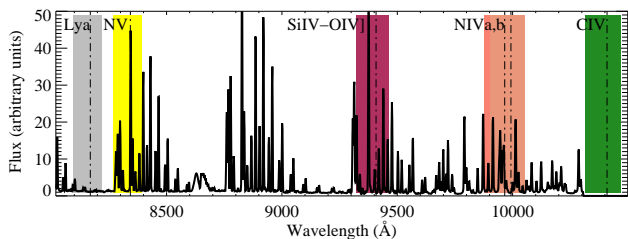


Figure 8. Sky spectrum and observed wavelength of typical emission lines produced in AGNs: N V, Si IV+O VI], N IV and C IV; with Ly α in the wavelength range of the NBC IV filter. The vertical dot-dashed lines correspond to the particular case of a galaxy at $z \sim 5.7$. No evidence of potential emission other than Ly α was found in the spectra (2D and 1D) of confirmed LAEs, although the spectra do not cover the wavelength of the C IV emission and most of the emission lines are in regions severely affected by sky lines.

4 COLOURS AND MAGNITUDES OF $z \sim 5.7$ LAES AND CONTAMINATION IN THE PHOTOMETRIC SAMPLE

4.1 Broad-band colours

The Ly α emission line can affect the broad-band colours of high redshift galaxies. In Paper I, we find that the $z \sim 6$ i' -dropout colour criterion is not a good tracer of galaxies at $z \sim 5.7$. The effect is more significant for objects with strong Ly α emission. The reason is that the i' -dropout selection is based on a condition of red ($i' - z'$) colour (e.g. $(i' - z') > 1.3$) and the Ly α emission of a galaxy at $z \sim 5.7$ would increase the flux in the i' -band therefore reducing the colour ($i' - z'$).

The spectroscopic data clearly confirms this expectation. Figure 9 shows the position of the photometric LAE candidates (black points) in the $(R_c - z')$ versus $(i' - z')$ colour diagram. Spectroscopically confirmed LAEs are indicated with blue circles and contaminants are indicated with red crosses. Open squares are the three LAE candidates in the field J1030+0524 observed with the 600ZD grating. The red dashed line is the $(i' - z') = 1.3$ colour boundary of the i' -dropout selection and only 4/33 LAEs reach this condition. Interestingly, the only spectroscopically confirmed LAE that satisfies the i' -dropout condition is LAE 103027+052419 (green star symbol), which is the closest LAE to the C IV absorption system at $z_{\text{C IV,b}} = 5.7242$ in the field J1030+0524 (see Section 7). The $(R_c - z')$ colours are only lower limits in the majority of the objects because they are non-detected in R_c . Nevertheless, most of them are detected in i' , which means that their $(i' - z')$ colours are more robust than their $(R_c - z')$ colours. For those objects that are non-detected in z' , the $(i' - z')$ colours are upper limits. In particular, the rows at $(R_c - z') = 0.86$ and 0.61 are made of objects only detected in i' and NBC IV.

Moreover, good agreement is found between our LAE sample and the confirmed LAEs at $z \sim 5.7$ from Shimasaku et al. (2006) (green open circles). This sample also shows bluer ($i' - z'$) than expected for i' -dropout, since none of them have $(i' - z') > 1.3$. The concentration of green circles around $(R_c - z') \sim 1.6$ and $(i' - z') = 0.4$ - 0.9 corresponds to non-detections in the R_c and z' bands, for which these colours are lower and upper limits, respectively. Keeping in mind that the $z \sim 5.7$ LAE selection is not defined in the

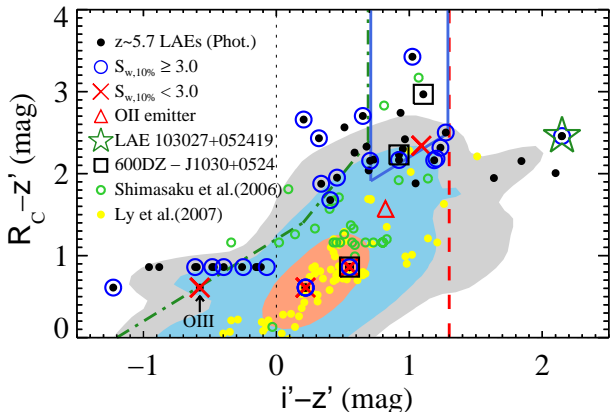


Figure 9. Broad-band $(R_c - z')$ versus $(i' - z')$ colours of the complete photometric sample of $z \sim 5.7$ LAEs (black points). The contours correspond to the photometric catalogue of detections and contain 50, 90 and 97 per cent of the sources in the catalogue. The spectroscopically confirmed LAEs ($S_{w,10\%} \geq 3.0$) are indicated with blue circles, and the contaminants ($S_{w,10\%} < 3.0$) are indicated with red crosses. The open star symbol highlights LAE 103027+052419 (see Section 7). The red dashed vertical line is the $(i' - z') = 1.3$ boundary condition for i' -dropouts, the blue solid lines indicate the colour criteria for $z \sim 5.7$ LBGs of Paper I. and the green dot-dashed line shows the colour selection for $z \sim 5.0$ LBGs of Ouchi et al. (2005a). Green open circles are SDF LAEs (Shimasaku et al. 2006) and solid yellow circles are lower redshift emitters in SDF from Ly et al. (2007).

colour-colour diagram of Figure 9, it is encouraging that the broad-band colours of the LAE sample agree with the expectations from the spectrophotometry of composite spectra of LBGs used to define the $z \sim 5.7$ LBG selection of Paper I.

The red open triangle is the O II emitter presented in Figure 4 and is found below the colour selection window for $z \sim 5.7$ LBGs (blue solid lines), in agreement with the contamination from low redshift galaxies analysed in Paper I. The colours of low redshift ($z \sim 0.07$ - 1.47) narrow-band emitters from Ly et al. (2007) are represented by yellow solid circles. This sample contains O II, O III and H α emitters, which are the dominant contamination source in LAE searches. Moreover, the sample covers a redshift range larger than that covered by the NBC IV transmission curve. Figure 9 shows that lower redshift emitters do not occupy the broad-band colour-colour region of higher redshift LAEs. As a result, the discrepancy in the colour-colour distribution of interlopers and spectroscopically confirmed LAEs provides a good reason to expect a low fraction of contamination among the LAE photometric candidates.

4.2 Narrow-band colours and the LAE photometric selection criteria

Figure 10 presents the colour-colour diagrams where the LAE colour selection criteria are defined (green dashed lines). The photometric sample of LAEs (black points) was selected from a catalogue of robust detections ($S/N_{\text{NBC IV}} \geq 5$). They can be seen to the right and to the left of the vertical dashed lines because the condition on the broad-band colours of LAEs (Paper I) requires that either colour is ‘red’, or there is no detection in all three broad-bands:

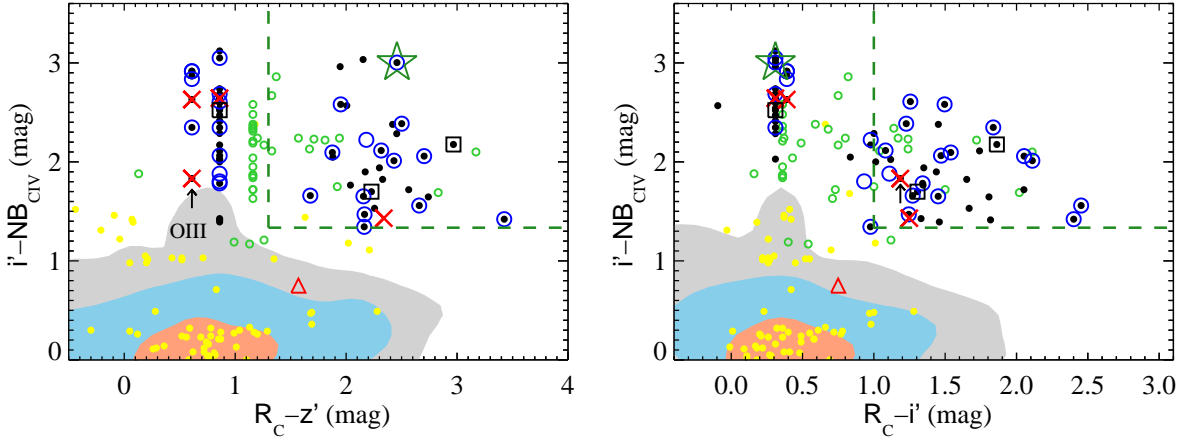


Figure 10. Broad-band colours and the excess in NBC IV. Symbol key is as per Figure 9. The green dashed lines show the boundaries of the LAE colour selection criteria. Objects non-detected in R_c and z' accumulate at $(R_c - z') = 0.86$ and 0.61 (left), and objects non-detected in R_c and i' accumulate at $(R_c - i') = 0.31$ and 0.39 (right).

$$[(R_c - i') > 1.0] \cup [(R_c - z') > 1.3] \cup [(R_c < 1\sigma) \cap (i' < 1\sigma) \cap (z' < 1\sigma)].$$

We have spectroscopic confirmation (blue circles) of photometric candidates. Those that show significant NBC IV excess but are not detected in more than one broad band are found at $(R_c - z') = 0.86$ and 0.61 (left hand panel), and at $(R_c - i') = 0.31$ and 0.39 (right hand panel). We recall that the majority of the objects are non-detected in R_c (see Tables A2 and A4) and therefore both $(R_c - i')$ and $(R_c - z')$ are lower limits.

The LAE discussed in Section 7 (LAE 103027+052419, open star symbol) is one of the objects at $(R_c - i') = 0.31$ which would have been missed if only one condition $(R_c - i') > 1.0$ (vertical green dashed line in the right hand panel) was applied. This means that the inclusion of the colour condition $\cup (R_c - z') > 1.3$ (vertical green dashed line in the left hand panel) in the selection of $z \sim 5.7$ LAEs is successful among objects like LAE 103027+052419 which are non-detected in the i' -band. Furthermore, we confirm five LAEs from the seven photometric candidates selected by the NBC IV excess but not detected in any broad-band, for which we have spectra with sufficient S/N (i.e. excluding the 600ZD data in the field J1030+0524). Figure 10 also shows $z \sim 5.7$ LAEs from SDF (Shimasaku et al. 2006) in green open circles. The narrow-band magnitude corresponds to the filter NB816, which is similar to NBC IV. Thus, when the measured magnitudes are compared, we consider them equivalent. We note that the selection criteria of these objects were based on their $(R_c - z')$ colour and, therefore, many of them do not reach $(R_c - i') > 1.0$. Since $z \sim 5.7$ LAEs are faint broad-band sources typically non-detected in R_c , we find objects that are only detected in one broad-band (i' or z'), or non-detected in all three broad-bands, by using a flexible broad-band colour condition (based on an ‘OR’ operator) in the selection criteria.

Objects with $S_{w,10\%} < 3.0$ (red crosses) do not seem to occupy a defined region. The red open triangle that indicates the colours of the O II emitter discussed in Section 3.2 is below the colour selection condition $(i' - \text{NBC IV}) = 1.335$ and bluer than $(R_c - i') > 1.0$. This is in agreement with the distribution of lower redshift emitter from Ly et al. (2007)

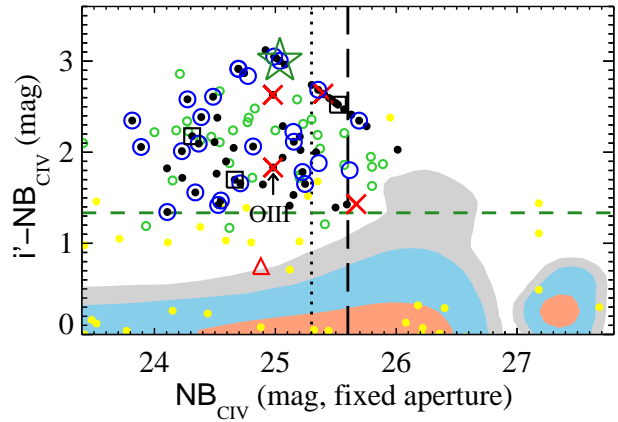


Figure 11. Colour-magnitude diagram ($i' - \text{NBC IV}$) versus NBC IV. Vertical lines indicate the NBC IV 5σ limiting magnitudes in the field J1030+0524 (dashed) and the field J1137+3549 (dotted).

(yellow circles), whose narrow-band magnitude corresponds to NB816. As a result, we find that lower redshift emitters have less significant narrow-band ($i' - \text{NBC IV}$) excess.

The colour-magnitude diagram ($i' - \text{NBC IV}$) versus NBC IV in Figure 11 shows that the O II emitter is among other lower redshift emitters from Ly et al. (2007) which can have brighter narrow-band magnitudes than the LAE sample. Moreover, it is clear that spectroscopically confirmed LAEs (including SDF LAEs) have larger ($i' - \text{NBC IV}$) colours than the contaminant population. In particular, we note that SDF LAEs and our LAE sample are evenly distributed and mixed in the colour-magnitude diagram ($i' - \text{NBC IV}$) versus NBC IV, meaning that both samples have similar brightness and colours.

In summary, our results validate the colour selection criteria for $z \sim 5.7$ LAEs of Paper I and suggest low contamination among bright ($\text{NBC IV} < 25$ mag) photometric LAE candidates.

5 SPECTROSCOPIC REDSHIFT DISTRIBUTION

Figure 12 shows the wavelength distribution of the Ly α peak emission of all the detections and the NBC IV filter transmission curve for comparison. The solid line includes all the objects in both fields and the grey histogram correspond to objects with $S_{w,10\%} \geq 3.0$. We find that the wavelength distribution is biased towards the blue half of the filter curve. This effect has been found in all previous narrow-band selected samples of high-redshift LAEs (e.g. Shimasaku et al. 2006; Ouchi et al. 2008; Kashikawa et al. 2011). The reason is that the flux contribution from the red side of the Ly α emission to the NBC IV magnitude decreases towards higher redshift. If the emission is bluer than the middle point of the NBC IV transmission curve (maximum throughput), the red wing of Ly α is covered by a more sensitive section of the filter and there is more rest-frame UV flux under the filter transmission curve. If the emission is redder than the middle point of the NBC IV transmission curve, there is little rest-frame UV flux included in the NBC IV magnitude, and the red wing of the Ly α is covered by a progressively less sensitive section of the filter.

Considering that Ly α is a resonant transition, radiative transfer plays a very important role in the escape of Ly α photons. Cosmological hydrodynamical simulations combined with radiative transfer have shown the effect of the dynamics of the surrounding H I gas (CGM and/or IGM) in the emission line profile. For example, Zheng et al. (2010) find that radiative transfer is needed to properly model frequency diffusion in which Ly α photons close to the central wavelength diffuse out to the wings of the emission line. The implication of this effect in the observed Ly α profile is clearly seen in Figure 5 of Zheng et al. (2010). They show simulated observations of Ly α profiles at $z \sim 5.7$ in which the emission peak is at a longer wavelength than the peak of the intrinsic profile. Moreover, the flux at the centre of the line is strongly suppressed, which results in an observed emission profile fully contained red-wards of the true line centre (e.g. Jensen et al. 2013).

Because we are aware that redshift estimates from the Ly α line are affected by the H I content of the near environment of the source and its kinematics, to measure the spectroscopic redshift of a $z \sim 5.7$ LAE, we prefer to use the bluest pixel of the line profile with flux over the 1σ level instead of the pixel with maximum flux, which is usually adopted in the literature (e.g. Ouchi et al. 2005a; Shimasaku et al. 2006; Hu et al. 2010). Our choice should bring our measurement in closer agreement with the true redshift of the galaxy.

The bottom panel of Figure 12 shows the redshift distribution of the LAEs in each field with line-filled histograms: black lines for J1030+0524 and red lines for J1137+3549. We notice that the redshift distribution is roughly centred at $z \sim 5.7$, which is lower than the redshift of the C IV absorption systems reported in the two lines of sight. The redshift of the C IV systems are indicated by the vertical lines: dot-dashed black line and dotted black line for the two C IV systems in the field J1030+0524 and dashed red line for the C IV system in the field J1137+3549.

The position of the emission under the narrow-band filter transmission curve depends on the redshift of an ob-

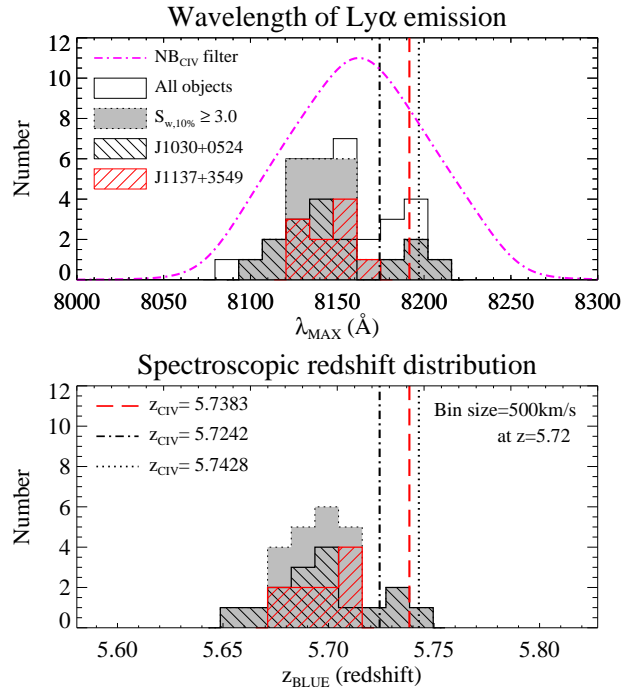


Figure 12. *Top:* Wavelength distribution of the maximum of the emission line of all the LAE candidates in both fields (black solid histogram). The grey filled histogram corresponds to candidates with $S_{w,10\%} \geq 3$ in both fields. Individual fields are shown by the black-line filled histogram (J1030+0524) and red-line filled histogram (J1137+3549). The vertical lines indicate the wavelength of Ly α at the redshift of the C IV absorption systems in each field, black dot-dashed and black dotted lines for the field J1030+0524 and red dashed for the field J1137+3549. *Bottom:* Spectroscopic redshift distribution of confirmed LAEs ($S_{w,10\%} \geq 3$), as measured from the bluest pixel of the emission line with flux above the 1σ level. Histogram key is the same as the top panel.

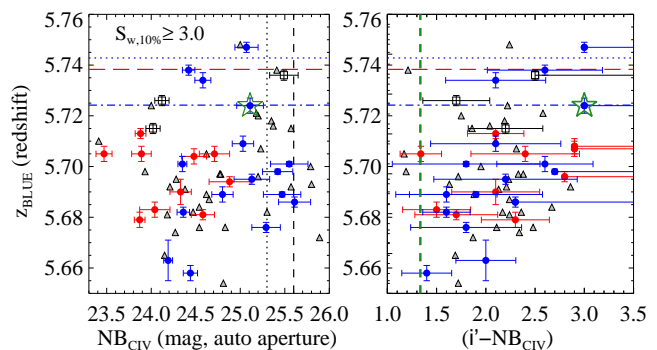


Figure 13. Narrow-band photometry versus spectroscopic redshift of emission lines with $S_{w,10\%} \geq 3.0$. Blue and red circles correspond to the two fields J1030+0524 and J1137+3549, respectively. LAE 103027+052419 is highlighted with a star symbol. Grey triangles are SDF LAEs (Shimasaku et al. 2006). The open squares represent the low resolution data (i.e. 600ZD grating) in the field J1030+0524, and although the sensitivity is not enough, if the emission is Ly α , these objects will fill the top half of the plots which are less populated.

ject. We searched for potential correlation between redshift and the narrow-band magnitude and colour and find no ob-

vious trend. Figure 13 presents the redshift of the LAEs as a function of the NBC IV magnitude (MAG_AUTO) and the (i' -NBC IV) colour (MAG_APER). Red circles correspond to LAEs in the field J1137+3549 and are contained in the range $z \sim 5.68$ – 5.72 , as in Figure 12, showing no correlation with NBC IV. Blue circles correspond to the field J1030+0524 and cover a wider redshift range $z \sim 5.66$ – 5.75 . Also in this case, the apparent magnitudes of the objects in the sample do not show a dependence with redshift.

The horizontal lines indicate the redshift of the C IV systems using the same line style as per Figure 12. The LAE indicated with the star symbol is LAE 103027+052419 at $z = 5.724 \pm 0.001$ (Section 7). The right hand panel of Figure 13 shows the spectroscopic redshift of the LAEs versus the NBC IV excess (i' -NBC IV). We note there seems to be a weak trend for higher redshift objects to have larger narrow-band excess. However, large photometric errors and several non-detections in the i' -band prevent us to reach a meaningful conclusion. Finally, we include $z \sim 5.7$ LAEs from SDF and find very good agreement with the distribution of our sample.

In summary, the distribution in redshift of the spectroscopic sample of LAEs is centred at $z \sim 5.7$ and no strong relation is found between the redshift and the narrow-band photometry of the LAE sample. Moreover, SDF LAEs at $z \sim 5.7$ show a distribution similar to our sample in the z versus NB and z versus (i' -NB) planes (Figure 13).

6 THE LARGE-SCALE ENVIRONMENT OF C IV ABSORPTION SYSTEMS

This section presents the spatial distribution of the complete LAE photometric sample based on spectroscopic information.

Figure 14 shows the projected distribution of LAEs in the fields J1030+0524 (left hand panel) and J1137+3549 (right hand panel) in comoving Mpc with respect to the C IV lines of sight, indicated by the black star and white star, respectively. Photometric LAE candidates are represented by open circles whose sizes indicate the NBC IV magnitude in the range 23.0–26.0 mag, in bins of 0.5 mag, with smaller circles for fainter objects. Squares indicate spectroscopic confirmation of LAEs ($S_{w,10\%} \geq 3.0$), and although most of them are photometric candidates (circles), the few squares without a circle correspond to object that are not included in the photometric sample because the S/N in the NBC IV band is slightly below 5. These objects are included in the analysis of the density contrasts. Finally, the red crosses are contaminants ($S_{w,10\%} < 3.0$), which are not included in the density contrast.

Following the analysis in Paper I, the contours in Figure 14 correspond to constant levels of density contrast $\Sigma_{\text{LAE}}/\langle\Sigma\rangle_{\text{LAE}}$, where $\langle\Sigma\rangle_{\text{LAE}}$ is the mean surface density averaged over the size of the field and Σ_{LAE} is the surface density of LAEs obtained using $1h^{-1}$ comoving Mpc bin size and a Gaussian smoothing kernel with FWHM = $10h^{-1}$ comoving Mpc. Solid contours correspond to over-dense regions, dashed contours correspond to mean density regions and dotted contours correspond to under-dense regions.

In the field J1030+0524 (left hand panel), the contours include all the photometric LAE candidates plus the

spectroscopy-only LAEs. The spectroscopic campaign confirms the projected structure reported in Paper I. The line of sight to the C IV system is found in a projected over-density of LAEs of $\Sigma_{\text{LAE}}(10)/\langle\Sigma\rangle_{\text{LAE}} \sim 1.5$, where the surface density within $10h^{-1}$ comoving Mpc radius is $\Sigma_{\text{LAE}}(10) = 89 \times 10^{-3}$ gal./arcmin², and the mean surface density of the field is $\langle\Sigma\rangle_{\text{LAE}} = 58 \times 10^{-3}$ gal./arcmin². In the field J1137+3549 (right hand panel), the distribution reported in Paper I is also confirmed. After removing contaminants, the surface density of the field is $\langle\Sigma\rangle_{\text{LAE}} = 16 \times 10^{-3}$ gal./arcmin². Within $10h^{-1}$ comoving Mpc the number of LAEs is so $\Sigma_{\text{LAE}}(10) = 36 \times 10^{-3}$ gal./arcmin². As a result, the revised density contrast increased to $\Sigma_{\text{LAE}}(10)/\langle\Sigma\rangle_{\text{LAE}} \sim 2.2$.

6.1 Distribution of $z \sim 5.7$ LAEs in the line of sight

The projected distribution of LAEs shows an over-density towards each C IV line of sight. However, spectroscopic follow-up suggests that the photometric LAE sample is at a slightly lower redshift than the C IV system in the J1137+3549 field (Figure 12). This result is clear in Figure 15 showing the projected distance (R) versus the radial velocity (Δv) to the corresponding C IV system in each field. Red solid circles and blue solid circles are spectroscopic LAEs in the field J1137+3549 and the field J1030+0524, respectively. Open squares are LAE candidates in the field J1030+0524 observed with the 600ZD grating (assuming that the emission is Ly α). Projected distances are measured from the position of the corresponding C IV line of sight, and radial velocities are measured respect to the C IV system at $z_{\text{C IV}} = 5.7242$ for J1030+0524 LAEs and the C IV system at $z_{\text{C IV}} = 5.7383$ for J1137+3549 LAEs.

The LAEs in the field J1137+3549 are at $17.9 \pm 6h^{-1}$ comoving Mpc in the line of sight direction ($\langle z \rangle_{\text{LAEs}} = 5.698 \pm 0.013$, $\langle \Delta v \rangle = -1784.6 \pm 585.9$ km s⁻¹) from the C IV system. Figure 15 shows that all the red circles are at > 1000 km s⁻¹ from the C IV system in the field. Thus, the photometric LAE sample is not in the immediate environment of the C IV system at $z = 5.7383$. Consequently, we cannot test the idea that the C IV system is associated with LAEs with our current data. Instead it should be tested with NB photometry better centred at the wavelength of the Ly α emission at $z = 5.7383$. Nevertheless, our spectroscopic findings presented here do not negate the results based on photometry presented in Paper I because the narrow redshift range is very useful for the interpretation of the comparison of projected distributions of galaxies. In addition, no C IV system is found in the QSO's spectrum at the redshift of the LAE sample. Since the closest LAE is at ~ 7 transverse comoving Mpc to the line of sight region without C IV, this observation does not contradict the idea that C IV systems are preferentially detected near LAEs, as supported by the result in J1030+0524 where an LAE-C IV system pair has been confirmed.

In the field J1030+0524, we find that, except for one, all spectroscopically confirmed LAEs are at $\gtrsim 5h^{-1}$ comoving Mpc from the C IV system in the line of sight direction ($|\Delta v| \gtrsim 500$ km s⁻¹). This LAE is represented by the green open star symbol and is at the same redshift as the high-column density C IV absorption system in the field.

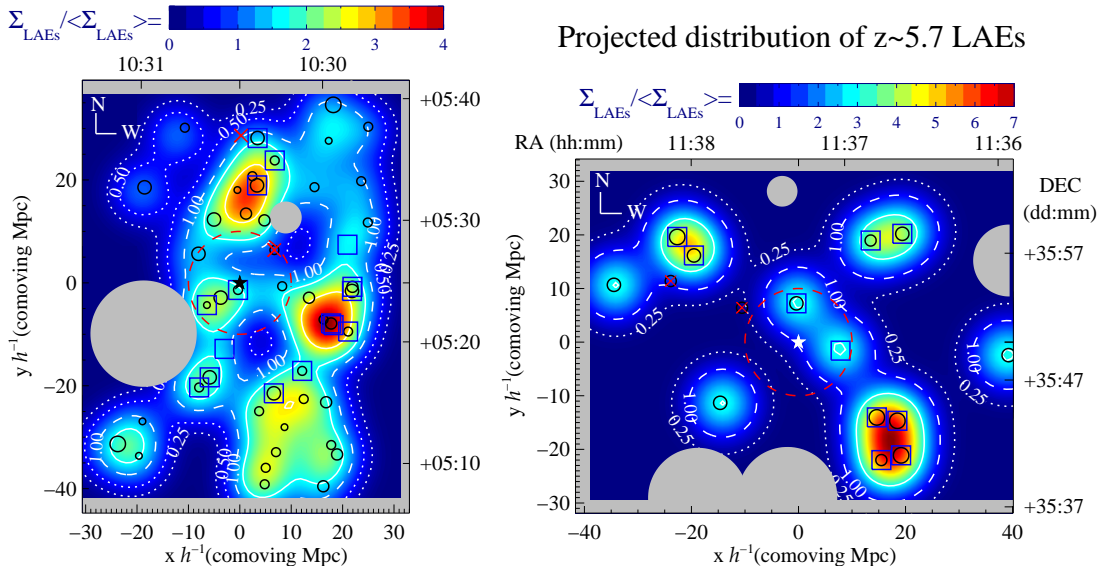


Figure 14. Projected distribution of LAEs in the field J1030+0524 (*left*) and the field J1137+3549 (*right*). Open circles are photometric candidates and the size of each circle indicates the apparent magnitude bin with larger circles for brighter magnitudes. Open squares are confirmed by spectroscopy ($S_{w,10\%} \geq 3.0$) and red crosses are non-LAEs ($S_{w,10\%} < 3.0$). The star symbol indicates the line of sight to the C IV systems and the red dashed circle centred on the star symbol has a radius of $10h^{-1}$ comoving Mpc. Masked areas of the field (bright Galactic stars and edges of the CCD) are shaded grey. The colour-coded contours correspond to constant levels of surface density contrast $\Sigma/\langle\Sigma\rangle$, obtained using $1h^{-1}$ comoving Mpc bin size and a Gaussian smoothing kernel with FWHM of $10h^{-1}$ comoving Mpc. Dotted contours correspond to under-dense regions ($\Sigma/\langle\Sigma\rangle < 1$), solid contours correspond to over-dense regions ($\Sigma/\langle\Sigma\rangle > 1$), and dashed contours correspond to mean density regions ($\Sigma/\langle\Sigma\rangle = 1$).

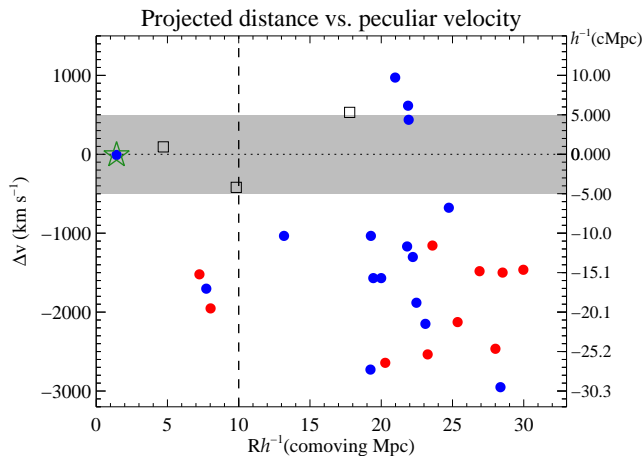


Figure 15. Projected distance to the C IV system measured from the position of the corresponding C IV line of sight, versus radial velocity measured respect to the C IV system at $z_{\text{C IV}} = 5.7242$ for J1030+0524 LAEs and the C IV system at $z_{\text{C IV}} = 5.7383$ for J1137+3549 LAEs. Blue and red circles correspond to confirmed LAEs in the field J1030+0524 and J1137+3549, respectively. The only confirmed LAE within $\pm 500 \text{ km s}^{-1}$ (star symbol) is the closest object at $212.8h^{-1}$ physical kpc. Open squares are LAEs observed with the 600ZD grating in J1030+0524. Although the data prevent a solid confirmation/rejection of these LAE candidates, we note that the position of the emission line put two of them within $\pm 500 \text{ km s}^{-1}$ from the C IV at $z_{\text{C IV}} = 5.7242$.

This galaxy-C IV system pair is presented with more detail in the next section. The mean redshift of the sample

is $\langle z \rangle_{\text{LAEs}} = 5.702 \pm 0.025$ ($\langle \Delta v \rangle = -989 \pm 1131 \text{ km s}^{-1}$), which shows that the sample is slightly biased towards lower redshifts. However, this value does not include the 600ZD grating data plotted as open squares. Interestingly, two of these objects are within $10h^{-1}$ comoving Mpc of projected distance and $\pm 500 \text{ km s}^{-1}$ of radial velocity. Although the main spectroscopic data set does not show an over-density in the line of sight direction at the position of the C IV system, if the tentative detections on the low resolution data are confirmed to be Ly α , then three out of the five LAEs within $10h^{-1}$ projected comoving Mpc are in the near environment of the C IV absorption ($|\Delta v| \lesssim 500 \text{ km s}^{-1}$). Considering the depth sampled by the LAE selection ($\sim 40h^{-1}$ comoving Mpc), the confirmation of the low resolution data will imply an over-density at $10h^{-1}$ comoving Mpc scale of $(3/10)/(5/40) \sim 2.4$, where five LAEs are detected in $\sim 40h^{-1}$ comoving Mpc depth of which three are within $\sim 10h^{-1}$ comoving Mpc depth. In conclusion, if the emission lines in the low resolution data of the field J1030+0524 are found to be Ly α , it will confirm that the C IV system is associated with an excess of LAEs.

7 SPECTROSCOPIC CONFIRMATION OF AN LAE-C IV ABSORPTION SYSTEM PAIR AT $z \sim 5.7$

One of the motivations to study the fields J1030+0524 and J1137+3549 is the search for galaxies physically connected to the C IV absorption systems. In this work, we report the redshift of LAE 103027+052419 (#4 in Figure 2) to be $z_{\text{Ly}\alpha} = 5.724 \pm 0.001$ measured at the position of the bluest

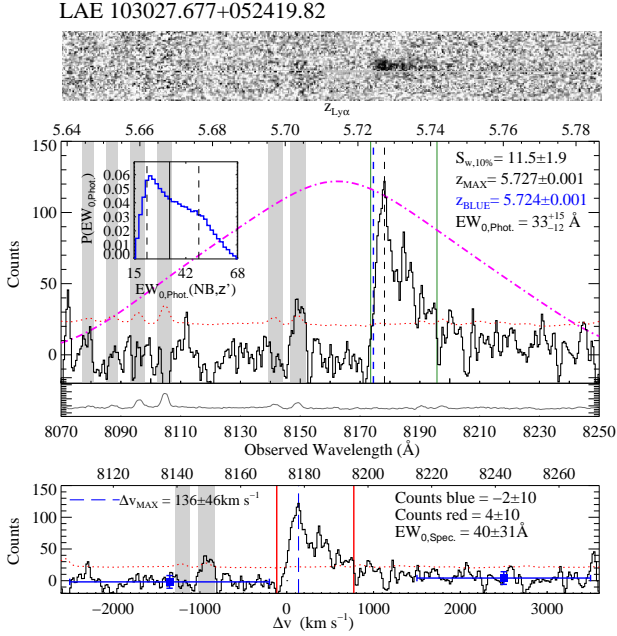


Figure 16. *Top:* Snapshot of the 2D slit spectrum in the wavelength range covered by the NBC IV filter. *Middle:* 1D spectrum of the emission line. The red dotted line indicates one standard deviation of the counts in the extraction box (1σ error), the magenta dot-dashed line is the scaled transmission curve of the NBC IV filter, the vertical dashed lines indicate the position of the maximum (black line) and the bluest pixel (blue line), and the grey shaded areas show the wavelength of the skylines where residuals can be large. The sky spectrum in arbitrary scale is given for reference in the bottom plot. The weighted skewness is measured in the range contained by the vertical green solid lines that indicate $\lambda_{10\%,B}$ and $\lambda_{10\%,R}$. *Inset:* Equivalent width probability distribution obtained from the photometry and the redshift of the object (see Section 8). The solid line and the dashed lines indicate the central value of the distribution (33 \AA) and the range enclosing a probability of 0.68, respectively. *Bottom:* Velocity with respect to the bluest pixel above 1σ . The vertical dashed line indicates the position of the emission peak, and the vertical dotted line and dot-dashed line show the velocity of the two CIV systems at $z_{CIV,b} = 5.7242$ and $z_{CIV,c} = 5.7428$ (Ryan-Weber et al. 2009; Simcoe et al. 2011; D’Odorico et al. 2013).

pixel of the emission line with $S/N = 1$, as a proxy for the centre of the intrinsic Ly α line. This confirms that the LAE is at $212.8h^{-1}$ physical kpc from a high column density CIV absorption system at $z_{CIV,b} = 5.7242 \pm 0.0001$.

Figure 16 presents a closer view of the spectrum of LAE 103027+052419. The emission line shows a clear asymmetry that is quantified by a weighted skewness of $S_{w,10\%} = 11.5 \pm 1.9$. The vertical green solid lines (middle panel) indicate the wavelength range $\lambda_{10\%,B} - \lambda_{10\%,R}$ used to measure $S_{w,10\%}$. The maximum of the emission is indicated by the black vertical dashed line at 8178 \AA , which corresponds to $z_{MAX} = 5.727 \pm 0.001$. However, the blue edge of the Ly α emission is very sharp whereas the red wing extends for at least 500 km s^{-1} suggesting that the line centre is bluer than the observed maximum of the emission.

The rest-frame equivalent width of Ly α obtained from the photometry is $EW_0 = 33^{+15}_{-12}\text{ \AA}$, which is the lowest EW_0

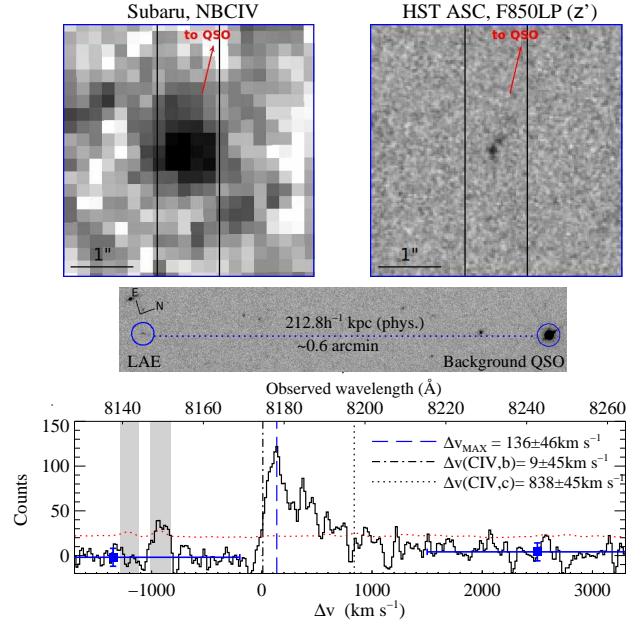


Figure 17. *Top:* Thumbnails (4×4 arcsec) of LAE 103027+052419 in NBC IV with Suprime-Cam on the Subaru Telescope (left) and F850LP (z') with ACS onboard HST (right). The black lines are the edges of the slit projected on the sky. The direction towards the background QSO is indicated with red arrows. The galaxy is distorted and elongated in the direction towards the background QSO. *Middle:* ACS image in the z' -band showing the projected distance from LAE 103027+052419 to the QSO line of sight. *Bottom:* Spectrum in km s^{-1} with respect to the bluest pixel above 1σ . The vertical dashed line indicates the position of the emission peak, and the vertical dotted line and dot-dashed line show the velocity of the two CIV systems at $z_{CIV,b} = 5.7242$ and $z_{CIV,c} = 5.7428$ (Ryan-Weber et al. 2009; Simcoe et al. 2011; D’Odorico et al. 2013).

of the LAE sample in the field J1030+0524 (see Section 8.2). This value is consistent with the spectroscopic measurement of EW_0 . In the bottom panel of Figure 16, the blue squares with error bars at each side of the emission line show the mean count level of the continuum, where the vertical error bars indicate one standard deviation of the flux in counts and the horizontal error bars enclose the wavelength range used to estimate the mean. At both sides of the emission, we avoided regions of significant skyline residuals (grey areas). We measure $F_{\lambda 1210} = -2 \pm 10$ counts for the blue side of the emission, which is consistent with zero. For the red side of the emission, the flux level is $F_{\lambda 1225} = 4 \pm 10$ counts, which is also consistent with zero. Nevertheless, we estimate $EW_{0,Spec}$ of the observed emission within the vertical solid lines using the continuum level $F_{\lambda 1225}$ and we find $EW_{0,Spec} = 40 \pm 31\text{ \AA}$, where the dominant source of error is the uncertainty in the continuum.

The Ly α emission peak has an offset of $\Delta v_{MAX} = 136 \pm 45\text{ km s}^{-1}$ from the redshift defined by the observed blue edge of the line. This velocity shift is smaller than the typically observed velocity offset of Ly α with respect to the systemic redshift of $z \sim 2-3$ LAEs: $\langle \Delta v(\text{Ly}\alpha) \rangle = 217 \pm 29\text{ km s}^{-1}$ (Hashimoto et al. 2013). However, these two velocities are not directly comparable. On one hand, the velocity of Ly α with respect to the systemic redshift measured

from nebular emission is interpreted as evidence for gas motion in the galaxy (e.g. McLinden et al. 2011; Hashimoto et al. 2013). On the other hand, our measurement of Δv_{MAX} is used as an indicator of the ‘sharpness’ of the blue edge of the emission, meaning that smaller Δv_{MAX} corresponds to line profiles with a steeper blue side. This is affected by a combination of several factors likely dominated by (a) the neutral hydrogen content in the IGM in the line of sight to the LAE, (b) H I intrinsic to the LAE, and (c) outflowing gas. Although we cannot differentiate between these effects without knowing the systemic redshift, they are probably related since galactic scale outflows can affect the distribution of the neutral gas which regulates the escape fraction of Ly α photons. Thus, although Δv_{MAX} does not directly probe the speed of the outflowing gas, it is interesting to see how it compares in relation to the rest of the sample. This is discussed in Section 9.

Figure 17 presents 4×4 arcsec thumbnails of LAE 103027+052419 (top panels), showing the slit used for spectroscopy and the direction to QSO J103027+052455. The image in the F850LP band (which equates to z') obtained with the Advanced Camera for Surveys (ACS) onboard the *Hubble Space Telescope* (right hand panel) shows a distorted shape slightly elongated towards the background QSO. The close proximity of this LAE to the line of sight of the C IV absorption systems is shown in the middle panel of the figure, and the velocity of the two C IV systems near the galaxy are shown in the bottom panel. The dot-dashed line corresponds to the second C IV absorption system at $z \geq 5.5$ in this line of sight at $z_{\text{C IV,b}} = 5.7242 \pm 0.0001$ ($\log N_{\text{C IV}} = 14.52 \pm 0.08$, D’Odorico et al. 2013), with $\Delta v(\text{C IV}_b) = 9 \text{ km s}^{-1}$. The dotted line corresponds to C IV $_c$, at $z_{\text{C IV,c}} = 5.7428 \pm 0.0001$ ($\log N_{\text{C IV}} = 13.08 \pm 0.1$, D’Odorico et al. 2013), with $\Delta v(\text{C IV}_c) = 838 \text{ km s}^{-1}$.

In summary, the spectroscopic redshift of LAE 103027+052419 confirms that this galaxy is the closest neighbour to the highest column density C IV absorption system known to date at $z \geq 5.5$. In addition, the red side of the emission line is very extended and reaches the wavelength corresponding to Ly α at the redshift of the C IV $_c$ absorption system. This finding demonstrates that star-forming galaxies can be detected in close proximity to highly ionized metal absorption systems immediately after the EoR, leading the path to exploring in better detail the origin and the physical state of the absorbing gas.

8 EQUIVALENT WIDTH

8.1 Measures of the Ly α emission line at $z \sim 5.7$

The faint continuum of $z \sim 5.7$ LAEs is the main obstacle to obtaining precise spectroscopic measurements of EW_0 . Therefore, EW_0 is usually measured using narrow-band and broad-band photometry (e.g. Malhotra & Rhoads 2002; Hu et al. 2004; Shimasaku et al. 2006; Zheng et al. 2014). On one hand, if the broad-band overlaps with the narrow-band (e.g. i' and NBC IV), an estimate of the flux of the continuum requires the subtraction of the contribution of the Ly α emission and a correction for the IGM transmission, which are usually both unknown. On the other hand, if the broad-band is redder than the narrow-band containing Ly α (e.g.

z' and NBC IV), then no IGM correction and no Ly α correction are needed to estimate the continuum flux. In this work, we have tested both methods and the approaches by several authors. We find that using a non-overlapping broad-band tends to give stable results that are independent of the method, whereas using an overlapping broad-band is more sensitive to the corrections applied to the continuum flux density. Therefore, we adopt the EW_0 obtained from the z' and NBC IV using the following procedure.

The emission line flux was estimated from the NBC IV band and the continuum flux density was measured with the z' -band at $\lambda_{\text{rest}} \sim 1350 \text{ \AA}$. We follow the approach suggested by Zheng et al. (2014) and use the equations:

$$\frac{N}{W_N} = a_N(\lambda) \times \frac{F_{\text{Ly}\alpha}}{W_N} + b_N(\lambda) \times \frac{F_{\text{Ly}\alpha}}{\text{EW}_0 \times (1+z)} \quad (1)$$

$$\frac{Z}{W_Z} = b_Z \times \frac{F_{\text{Ly}\alpha}}{\text{EW}_0 \times (1+z)}, \quad (2)$$

where Z and N are the integrated fluxes in the z' -band and the NBC IV band, respectively; and W_N and W_Z are the corresponding filter width $W_N = \int T_N \delta\lambda / \max(T_N)$ and $W_Z = \int T_Z \delta\lambda / \max(T_Z)$, with T_Z and T_N representing the transmission curve of each filter. The observed Ly α flux is $F_{\text{Ly}\alpha}$ and the continuum flux density was replaced by $F_{\text{Ly}\alpha} / (\text{EW}_0 \times (1+z))$. Because the narrow-band filter is not a top-hat, the contribution of the Ly α line to the NBC IV flux depends on the filter transmission at the wavelength of the emission. The coefficient $a_N(\lambda)$ is a correction for this effect and is estimated as the ratio of the filter transmission at the wavelength of the emission line over the maximum transmission at the centre of the filter $a_N = T_N(\lambda_{\text{MAX}}) / \max(T_N)$. The Ly α emission is not covered by the z' -band, thus the first term of equation 1 is not present in equation 2. The correction for the IGM absorption to the continuum emission in the NBC IV and z' -bands is applied through b_N and b_Z . Since, the broad-band is redder than Ly α , no correction is necessary in z' , thus $b_Z = 1$. Considering that most of our LAEs are non-detected in R $_c$, we assume that the contribution from the continuum bluer than Ly α ($\lambda < \lambda_{\text{BLUE}}$) is negligible to flux measured by the narrow-band. Under this assumption b_N is calculated as the fractional area of the NBC IV transmission curve for $\lambda \geq \lambda_{\text{BLUE}}$: $b_N = \int_{\lambda_{\text{BLUE}}}^{\infty} T_N \delta\lambda / \int T_N \delta\lambda$, where λ_{BLUE} is the wavelength of the bluest pixel of the emission line. Finally, our measurements of the EW_0 only account for the observed Ly α flux since no correction for IGM absorption to the Ly α emission was applied. In summary, our approach uses the wavelength of the emission line to estimate the corrections for individual objects.

The expression for EW_0 from equations 1 and 2 is

$$\text{EW}_{0,\text{Phot.}} = \frac{N \times W_Z - Z \times b_N \times W_N}{Z \times a_N} \times \frac{1}{(1+z)}. \quad (3)$$

The equivalent width probability function $P(\text{EW}_0)$ of each LAE was obtained by Monte Carlo simulation. Values for the z' -band magnitude were pulled from a Gaussian distribution centred at the measured magnitude with a standard deviation equal to the magnitude error $\delta z'$. The same process was used to sample the NBC IV magnitude, and for each pair of values we calculate EW_0 . After 10^5 iterations, $P(\text{EW}_0)$ is obtained and from it we calculate the mean and

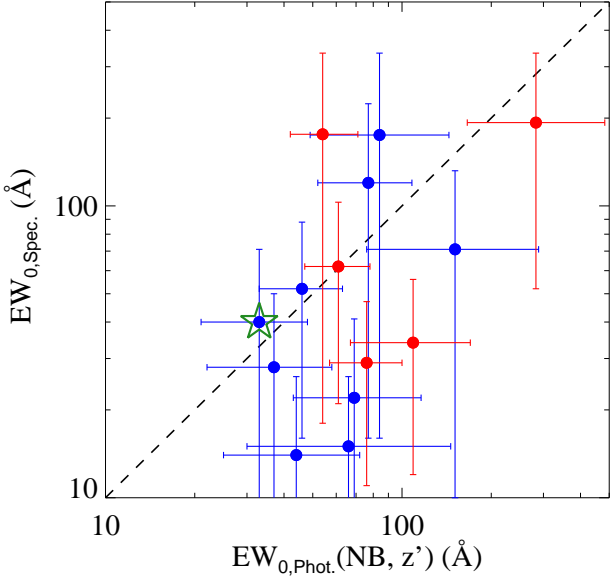


Figure 18. Comparison of the spectroscopic and photometric estimates of the rest-frame equivalent width (EW_0) of nine LAEs in the field J1030+0524 (blue circles) and five LAEs in the field J1137+3549 (red circles). Spectroscopy only provides upper limits for the remainder LAEs in the sample, which are not included in this figure. The dashed line is the identity relation 1:1. Points that depart from the identity towards lower spectroscopic values can result from the subtraction of sky emission lines affecting Ly α . The green star is LAE 103027+052419 (Figure 16) and is one of the examples showing agreement in the EW_0 measured with both methods.

the errors in EW_0 . Following Shimasaku et al. (2006), the central value EW_c is defined as $\int_0^{EW_c} P(EW_0)\delta EW_0 = 0.5$, and the 1σ upper and lower limits that contain 68 per cent of the distribution are estimated from $\int_{EW_-}^{EW_c} P(EW_0)\delta EW_0 = 0.34$, and $\int_{EW_c}^{EW_+} P(EW_0)\delta EW_0 = 0.34$, respectively. For objects non-detected in z' , lower limits in the EW_0 are calculated by adopting the 1σ limiting magnitude. These measurements are reported in Tables A1 and A3 in Appendix A. The equivalent width probability function of each LAE is plotted in Appendix B.

In the few examples where it was possible to measure EW_0 from the spectrum, we find that the agreement with the photometric estimates using the z' magnitude for the continuum is better than using the i' magnitude. Figure 18 compares the photometric and spectroscopic measurements of EW_0 of 14 LAEs. The vertical error bars are dominated by the uncertainty in the continuum flux density. In particular, some spectra are contaminated by light from other slits (shown in Figure 1), which is a source of error for the continuum determination. Moreover, the subtraction of sky emission lines can have a significant impact in the properties of a Ly α emission line by modifying the skewness, changing the position of the emission peak and diminishing the measured line flux. Thus, it is possible that the lower values measured from the spectra of the objects below the $x = y$ line (dashed line) are biased by these effects. Having said that, although $EW_{0,Spec}$ have large errors, we interpret our

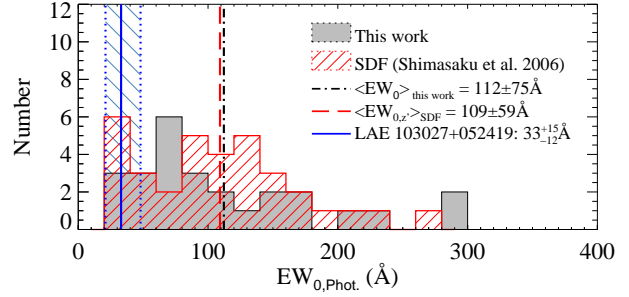


Figure 19. Rest-frame equivalent width distribution of confirmed LAEs in both fields (grey filled histogram). The red line hatched histogram corresponds to SDF LAEs (Shimasaku et al. 2006). The vertical lines indicate the mean value of each distribution, long-dashed for SDF LAEs and dot-dashed for our sample. The blue vertical line and line-filled region indicate EW_0 and 1σ uncertainty of LAE 103027+052419, which is clearly at the low end of the distribution.

results in Figure 18 as evidence that the photometric determination of EW_0 using a non-overlapping broad-band filter returns values that are supported by spectroscopy. Nevertheless, we recognise the need for deeper spectroscopy to consistently measure the properties of $z \sim 5.7$ LAEs.

8.2 Distribution of EW_0

Figure 19 presents the EW_0 distribution of the LAE sample of this work (grey histogram) and the LAE sample from SDF (Shimasaku et al. 2006, red-dashed histogram). We find agreement in the mean and the standard deviation of both samples. The equivalent width of LAE 103027+052419 is represented by a solid blue line and a blue-hatched region enclosing 68 per cent of the $P(EW_0)$. It is clear from this figure that LAE 103027+052419 has a lower EW_0 than the rest of the sample. This is interesting considering that lower redshift LAEs ($z = 2-3$) with lower EW_0 values tend to display larger velocity shifts of the Ly α emission peak with respect to the systemic redshift (e.g. Hashimoto et al. 2013). Moreover, the same effect is observed among LBGs (e.g. Adelberger et al. 2003; Shapley et al. 2003). The implications of this result are discussed in Section 10.

We compare the EW_0 with the NBC IV magnitude and ($i' - \text{NBC IV}$) colour of $z \sim 5.7$ LAEs in Figure 20. Blue and red circles correspond to the samples of the present work and grey triangles correspond to SDF LAEs. In the left panel, we find no trend between EW_0 and NBC IV magnitude since both LAE samples are well distributed across the plot. This is not a surprise because the NBC IV magnitude measures the flux of the emission line and part of the continuum while EW_0 is a relative measure of the flux in the emission line with respect to the continuum. A rough estimate of this relation is the ($i' - \text{NBC IV}$) colour which is slightly larger for LAEs with larger EW_0 (right panel of Figure 20). The open star symbol is LAE 103027+052419, and it seems to occupy a curious corner in the plot. This LAE is not detected in i' , so the colour is a lower limit. Usually, other non-detections in i' have larger EW_0 because they are also very faint in z' , what brings them into the relation. How-

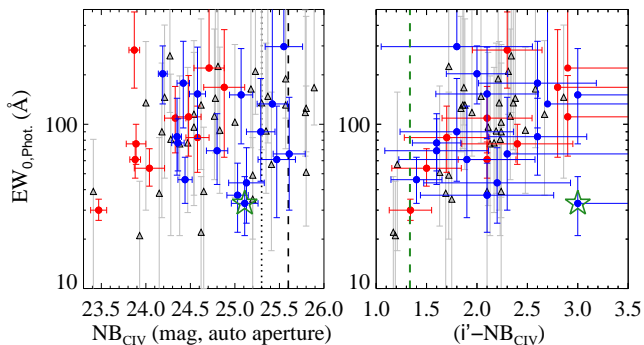


Figure 20. Narrow-band photometry versus EW_0 of confirmed LAEs. Blue and red circles correspond to the two fields J1030+0524 and J1137+3549, respectively. Triangles are SDF LAEs. LAE 103027+052419 is highlighted with a star symbol. *Left:* The magnitude in NBC_{IV} does not correlate with EW_0 . *Right:* The excess $(i' - NBC_{IV})$ shows a small trend with EW_0 in which LAEs with higher EW_0 have redder $(i' - NBC_{IV})$ colour. This is also seen in the SDF sample. Considering that both quantities are independent probes of the flux excess with respect to the continuum, the existence of this relation is reasonable and encouraging. However, large uncertainties limit the detection of a significant correlation.

ever, LAE 103027+052419 is brighter in z' than the other LAEs with lower-limit $(i' - NBC_{IV})$ colours, resulting in a lower EW_0 which is closer to the expectation for LBGs.

This is clearly seen in Figure 21 which presents M_{UV} versus EW_0 . Symbol key is the same as per previous figures. The open star representing LAE 103027+052419 is in the middle-bottom of the distribution and seems to agree with the trend previously noted by many authors that fainter UV galaxies at $z = 5-6$ have larger EW_0 (Ando et al. 2006; Shimasaku et al. 2006; Stanway et al. 2007; Ouchi et al. 2008). The remaining LAEs with lower-limit $(i' - NBC_{IV})$ colours are at the top-right corner of the Figure, that corresponds to large EW_0 and faint M_{UV} . The horizontal dotted line shows that only one LAE in our sample has a lower EW_0 than LAE 103027+052419.

In summary, the distribution of EW_0 is comparable with the sample of $z \sim 5.7$ LAEs from SDF, and the closest neighbour to C_{IV_b} (LAE 103027+052419) has one of the lowest EW_0 , which is well determined by photometry and spectroscopy.

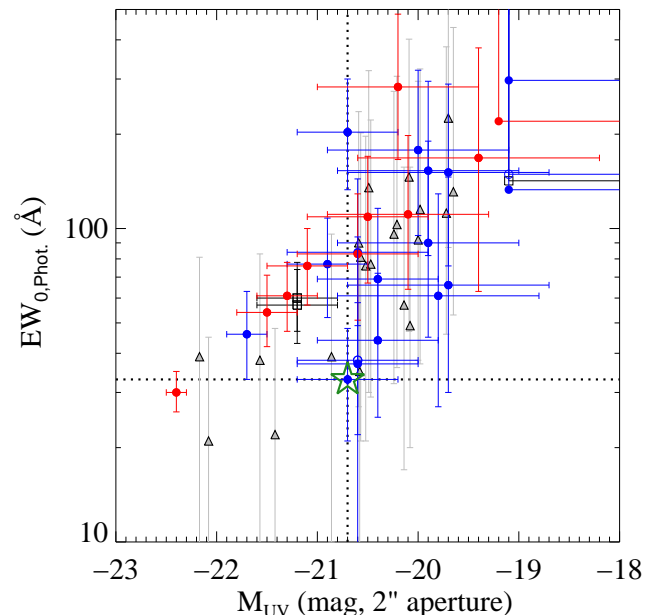


Figure 21. Absolute magnitude at $\lambda_{rest} \sim 1350 \text{ \AA}$ and EW_0 of confirmed LAEs. As in previous figures, blue and red circles correspond to the fields J1030+0524 and J1137+3549, respectively, and triangles are SDF LAEs. Both samples seem to follow the same relation where more luminous objects tend to have smaller EW_0 . LAE 103027+052419 is highlighted with a star symbol and the dotted lines (vertical and horizontal) show that fainter LAEs (i.e. to the right of LAE 103027+052419) have larger EW_0 (i.e. above LAE 103027+052419).

9 VELOCITY OF THE $Ly\alpha$ EMISSION PEAK

Many authors have found that the wavelength of the $Ly\alpha$ emission peak tends to be shifted from the systemic redshift of a galaxy, which is measured from nebular emission lines (Adelberger et al. 2003; Steidel et al. 2010; Finkelstein et al. 2011; McLinden et al. 2011; Hashimoto et al. 2013; Chonis et al. 2013; Shibuya et al. 2014). The velocity shift of the $Ly\alpha$ emission is interpreted as the result of the dynamics of the gas. In this study, we have no measurements of the systemic redshift from rest frame optical nebular lines, thus we have adopted the redshift of the bluest pixel of the $Ly\alpha$ emission as the best approximation to the real redshift of the galaxy. This section presents Δv_{MAX} , which is the velocity of the pixel with the maximum flux with respect to the redshift of the galaxy, and shows how it compares with other observables of LAEs such as the asymmetry of the emission line profile, the equivalent width and the UV luminosity.

Starting with the distribution of Δv_{MAX} , the top panel of Figure 22 shows that the mean velocity of the LAE sample is $\langle \Delta v_{MAX} \rangle = 118 \pm 56 \text{ km s}^{-1}$. The velocity shift measured in LAE 103027+052419 is $\Delta v_{MAX} = 136 \pm 45 \text{ km s}^{-1}$ which is higher than the mean of the sample but within one standard deviation. The rest of the section is dedicated to the possible dependencies of Δv_{MAX} with other observables plotted in Figure 22. The symbol key is the same we have used before, with the green star symbol representing LAE 103027+052419. The errors in Δv_{MAX} are very conservative since they are determined from the resolution of the obser-

vations (FWHM= 2.5 Å for the 830G data and 3.5 Å for the 600ZD data, Section 2).

The second panel from the top presents Δv_{MAX} versus redshift and no correlation is seen. This is not surprising since the factors that regulate the Ly α profile (e.g. speed of the gas, column density of the neutral gas, etc.) are not expected to evolve dramatically in the small redshift range of the LAE sample (~ 20 Myr). Moreover, if there was a trend with redshift it would suggest that Δv_{MAX} is not dominated by gas dynamics but by some observational systematic effect, which is not the case.

The resonant nature of Ly α implies that radiative transfer effects coupled with the dynamics of the gas result in spatial and wavelength diffusion of Ly α photons (Hansen & Oh 2006; Zheng et al. 2010; Dijkstra & Kramer 2012; Jeon-Daniel et al. 2012). In general, red-shifted Ly α photons find it easier to reach the observer than blue-shifted Ly α photons because they are not absorbed by the H I in the direction to the observer whereas the latter do. Furthermore, if the gas has an additional velocity component caused by some type of outflow mechanism, the Ly α photons reprocessed in the receding side of the outflow will also experience an additional redshift that will take them out of resonance allowing them to reach the observer (Ahn, Lee & Lee 2003; Verhamme et al. 2006; Dijkstra & Wyithe 2010). In this case, the observed line profile presents a red ‘tail’ –that may also show some structure or ‘bumps’– which increases its asymmetry. However, at fixed outflow velocities, larger H I column densities produce broader Ly α profiles and larger velocity shifts of the Ly α peak (e.g. Figure 1 of Verhamme et al. 2014) which would reduce the asymmetry of the line profile.

In the middle panel of Figure 22 (labeled C), there is a weak suggestion that the weighted skewness defined in Section 3.2 increases with Δv_{MAX} . Considering that $S_{w,10\%}$ measures the asymmetry of the line profile, this observable increases for a more extended ‘red wing’ and sharper ‘blue edge’. Because Δv_{MAX} is a measurement of the extent of the blue edge of the emission, a smaller Δv_{MAX} correspond to a sharper blue edge. Therefore, a smaller Δv_{MAX} should result in a more asymmetric profile, i.e. larger $S_{w,10\%}$. However, the opposite relation is observed since $S_{w,10\%}$ increases with Δv_{MAX} . This could indicate that the extension of the red wing may correlate, although slightly, with the shift of the Ly α peak to longer wavelengths.

As mentioned before, since outflowing gas would enhance the extension of the red wing of the emission, then a galactic wind would increase $S_{w,10\%}$ with respect to the case without it. In addition, larger H I column densities produce greater redward shifts of the Ly α peak, although reducing the asymmetry of the profile. The tentative trend in panel (C) indicates that larger H I column densities (larger Δv_{MAX}) might also host stronger galactic outflows (larger $S_{w,10\%}$). Under this picture, since LAE 103027+052419 has a large Δv_{MAX} and one of the a largest weighted skewness of the sample, it is possible that this galaxy contains a stronger outflow and a larger H I column density compared to the rest of the LAE sample.

Panel D shows Δv_{MAX} versus EW_0 where LAE 103027+052419 is among the lowest EW_0 and the highest Δv_{MAX} . This is in agreement with lower redshift observations that LAEs and LBGs with higher EW_0 tend to have lower Ly α velocity shifts (e.g. Shapley et al. 2003; Shibuya et

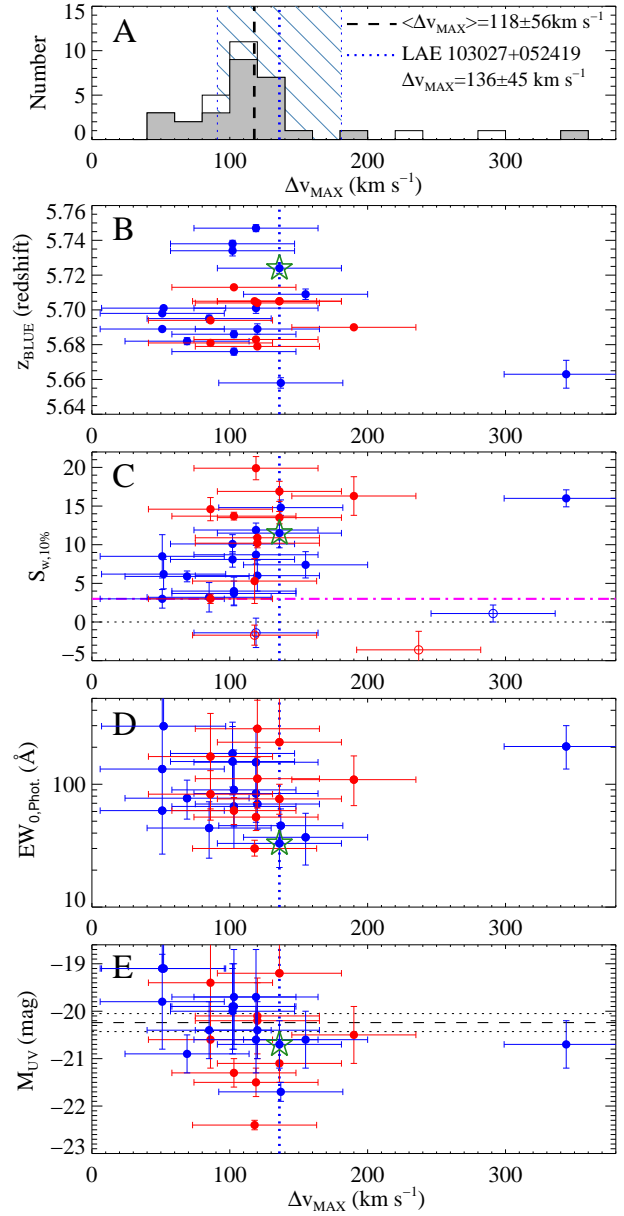


Figure 22. The velocity of the Ly α emission maximum is plotted against other properties. The errors in Δv_{MAX} are conservatively large as they were estimated from the FWHM of the data in the dispersion direction (2.5–3.5 Å). Blue and red circles correspond to the fields J1030+0524 and J1137+3549, respectively, and LAE 103027+052419 is highlighted with a star symbol. (A) Distribution of Δv_{MAX} including both fields. The complete sample of candidates is plotted with the solid line histogram and the sample of confirmed LAEs is plotted with a grey filled histogram. The dotted vertical line is LAE 103027+052419 and is found in the high velocity half of the distribution. (B) Δv_{MAX} versus redshift shows no correlation. (C) Δv_{MAX} versus $S_{w,10\%}$. A small trend might be present in which high skewness LAEs have larger Δv_{MAX} than low skewness LAEs. (D) Δv_{MAX} versus EW_0 shows that LAE 103027+052419 has one of the lowest EW_0 and is among the highest Δv_{MAX} . (E) Δv_{MAX} versus M_{UV} shows that LAE 103027+052419 is close to $M_{\text{UV}}^*(z = 6.0)$ (horizontal dashed line) and galaxies with higher Δv_{MAX} have similar M_{UV} .

al. 2014). However, the scatter shown by our data prevents us from identifying any trend.

Finally, the bottom plot (panel E) presents M_{UV} versus Δv_{MAX} and shows that the galaxies with the largest Δv_{MAX} values have similar M_{UV} to LAE 103027+052419 and close to (or larger than) M_{UV}^* (-20.24 ± 0.19 mag, Bouwens et al. 2007, horizontal dashed line). Once again, this result is in agreement with statistics of outflows in lower redshift galaxies which have found larger wind speed in more massive galaxies (e.g. Martin 2005; Weiner et al. 2009; Bradshaw et al. 2013). Furthermore, LAEs at $z \sim 2-3$ show smaller velocity offset than bright LBGs (McLinden et al. 2011, 2014; Chonis et al. 2013; Hashimoto et al. 2013; Shibuya et al. 2014). Interestingly, if more massive star-forming galaxies at $z \sim 5.7$ contain larger H I column densities, then it is logical to expect that, statistically, UV brighter galaxies (i.e. more massive) have larger Δv_{MAX} , lower EW_0 and stronger outflows which result in more asymmetric profiles (larger $S_{w,10\%}$).

In summary, LAE 103027+052419 presents one of the largest values of Δv_{MAX} in the spectroscopic sample of LAEs. Although Δv_{MAX} is not a direct measure of the outflow speed and the errors in Δv_{MAX} are rather large, the tentative detection of trends with $S_{w,10\%}$, EW_0 and M_{UV} could reflect a dependence with the gas dynamics and/or the mass of the galaxy. As a result, the position of LAE 103027+052419 in the plots of Figure 22 suggest that this LAE is a good candidate to host galactic-scale outflows among the LAEs in the sample.

10 THE ORIGIN OF C IV ABSORPTION SYSTEMS AFTER THE EPOCH OF REIONIZATION

In this section we discuss the possibility that C IV_b is physically associated with LAE 103027+052419. The proximity in redshift confirms that these two object are close neighbours, thus the final question explored in this work is the possibility that the galactic scale wind of LAE 103027+052419 enriched its environment out to $\gtrsim 212h^{-1}$ physical kpc.

10.1 Evidence from the Ly α emission

The distribution and kinematics of the gas in a galaxy affects the escape of Ly α photons from the galaxy and the Ly α line profile (Hansen & Oh 2006; Verhamme et al. 2006, 2008; Dijkstra & Wyithe 2010; Zheng et al. 2010; Orsi, Lacey & Baugh 2012; Garel et al. 2012; Behrens, Dijkstra & Niemeyer 2014). In Figure 17, the two C IV absorption systems at $\sim 212h^{-1}$ projected kpc show small velocities with respect to the Ly α emission line of LAE 103027+052419. The strongest C IV system known at $z \gtrsim 5.5$, C IV_b, has a column density $\log N_{CIV} = 14.52 \pm 0.08$ and is found at 9 km s^{-1} from the LAE. The other C IV absorption system at a similar redshift, C IV_c, is weaker ($\log N_{CIV} = 13.08 \pm 0.1$) and is found at 838 km s^{-1} from the LAE, which is not too far from the red end of the Ly α emission.

The Ly α peak of LAE 103027+052419 is at $\Delta v_{MAX} = 136 \pm 45 \text{ km s}^{-1}$. Moreover, it has one of the lowest EW_0 values (Section 8) and one of the highest Δv_{MAX} values (Section 9) of the sample of LAEs in this study, which is in agreement

with the observed anti-correlation between EW_0 and $\Delta v_{Ly\alpha}$ in star-forming galaxies like LBGs and LAEs at $z \sim 2-3$ (e.g. Shapley et al. 2003; Hashimoto et al. 2013; Shibuya et al. 2014). In other words: larger velocity shifts are found among lower EW_0 . Radiative transfer studies (e.g. Verhamme et al. 2008, 2014) show that a higher neutral hydrogen column density results in a larger velocity shift of the Ly α peak. This is valid for outflow velocities $\lesssim 300 \text{ km s}^{-1}$ since larger velocities will allow Ly α photons to escape more easily closer to the line centre, thereby reducing $\Delta v_{Ly\alpha}$. Therefore, a low $\Delta v_{Ly\alpha}$ could result from a low column density of H I or a large outflow speed, whereas a large $\Delta v_{Ly\alpha}$ implies not only larger H I column densities but also lower outflow speeds.

This result is in agreement with Zheng et al. (2010) who find the radiative transfer of Ly α photons to be dominated by the density and velocity structures of the gas in the CGM and IGM. As a result, the wavelength of the Ly α peak tends to shift to longer wavelengths in more massive dark matter haloes. Given that more luminous galaxies at $z \sim 5.7$ are more massive (González et al. 2011; McLure et al. 2011), the trend for UV brighter LAEs to have larger Δv_{MAX} shown in the bottom panel of Figure 22 is consistent with this picture. Therefore, according to the UV luminosity, Ly α profile, Δv_{MAX} and EW_0 , it is possible that LAE 103027+052419 is at the high mass end of the LAEs, has a large H I column density, and is a good candidate for a large scale outflow.

10.2 The outflow scenario

Although the speed of the outflowing gas cannot be measured without the detection of nebular emission lines and ISM absorption lines in the continuum of the galaxy, the distance to the absorption system and the limit imposed by the age of the Universe can help us to understand the origin of the metals. The separation of the LAE-C IV system is estimated from the angular separation on the sky ($\delta\theta = 36.2412$ arcsec) and the corresponding redshifts as $d = \sqrt{D_A^2(z_{Ly\alpha}, z_{CIV,b}) + (\delta\theta D_M / (1 + z_{CIV,b}))^2}$, where $D_A(z_{Ly\alpha}, z_{CIV,b})$ is the angular diameter distance between the redshifts of the LAE and the C IV system and $\delta\theta D_M$ is the transverse comoving distance at the redshift of the C IV system. Figure 23 shows a diagram of the distance in the LAE-C IV system pair assuming the redshift z_{BLUE} and z_{MAX} and their uncertainties. The Figure clearly shows that the distance estimated from z_{BLUE} is close to the minimum distance, which is important when considering the time needed for an outflow to reach the position of the C IV system.

The time required for outflowing gas to reach a distance of $212.8h^{-1}$ kpc depends on the speed of the gas: a typical outflow speed of $\sim 200 \text{ km s}^{-1}$ would require a time longer than the age of the Universe at $z = 5.724$. Therefore, if the carbon was produced in stars of LAE 103027+052419, the outflowing material had to have a larger mean velocity during its journey. For example, at $\sim 400 \text{ km s}^{-1}$ it would have taken 0.518 Gyr to travel $212h^{-1}$ kpc, implying that the outflow mechanisms were in place by $z \sim 10.1$. Figure 24 presents the time required for an outflow travelling at mean velocity ($V_{outflow}$) to reach $212.8h^{-1}$ physical kpc (solid line) and $282h^{-1}$ physical kpc (dotted line) corresponding to the separation determined using $z_{Ly\alpha} = z_{BLUE}$

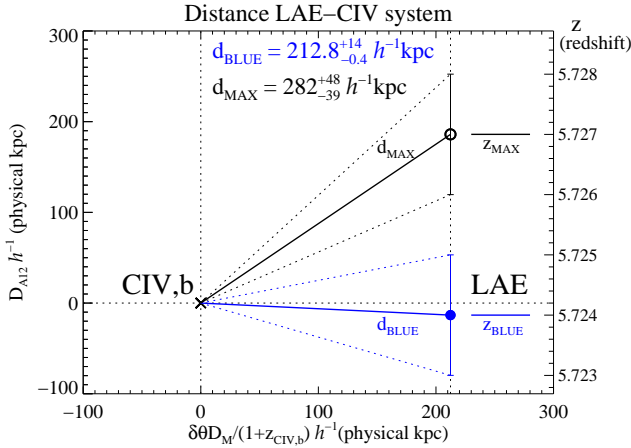


Figure 23. Distance from CIV,b to LAE 103027+052419. The x axis is the transverse distance $\delta\theta D_M / (1 + z_{CIV,b})$ where $\delta\theta = 36.2412$ arcsec is the angular separation on the sky. The y axis is the angular diameter distance D_A between $z_{LY\alpha}$ and $z_{CIV,b}$. The black open circle corresponds to $z_{LY\alpha} = z_{MAX}$ and the blue solid circle corresponds to $z_{LY\alpha} = z_{BLUE}$. The uncertainty on $z_{CIV,b}$ is an order of magnitude better than that of the LAE.

and $z_{LY\alpha} = z_{MAX}$, respectively. The age of the Universe at $z = 5.724$ (~ 0.97 Gyr) provides a hard limit for the mean outflow speed. However, theoretical studies predict that the formation of the first mini-haloes capable of hosting PopIII star-formation started around $20 < z < 30$ (e.g. Barkana & Loeb 2001; Yoshida et al. 2003; Gao et al. 2007; Bromm & Yoshida 2011). Moreover, the first systems that can be considered ‘galaxies’ are predicted to have formed around $10 < z < 20$ (e.g. Loeb 2010; Greif et al. 2010; Bromm & Yoshida 2011). These limits imply that it is practically impossible for a low speed outflow ($\langle V_{outflow} \rangle < 250 \text{ km s}^{-1}$) from LAE 103027+052419 to reach the position of the CIV absorption system. Mean outflow velocities in the range 250–400 km s^{-1} should have departed from the LAE during the assembly of the first stars and galaxies. Finally, a strong outflow ($\langle V_{outflow} \rangle > 400 \text{ km s}^{-1}$) would have had enough time to enrich the region if the outflow was active since $z \sim 10$. If the redshift of the galaxy is z_{MAX} , then the distance to the CIV system is $282h^{-1}$ physical kpc and stronger winds (additional $\sim 150 \text{ km s}^{-1}$ in the given examples) are required to reach the position of the CIV, which will make the ‘late-outflow’ scenario even less plausible.

A comparison with outflow velocities from the literature is shown in Figure 24. Verhamme et al. (2006) used 3D radiation transfer of Ly α photons and report that a model of an expanding shell of cold gas would produce a Ly α peak with a velocity shift of $\sim 2 \times V_{outflow}$, where $V_{outflow}$ is measured from the blueshift of inter-stellar absorption lines (IS). Under the assumption that Δv_{MAX} is the velocity shift of the Ly α peak with respect to the systemic redshift, the outflow speed would be $\frac{\Delta v_{MAX}}{2} \sim 68 \text{ km s}^{-1}$ (magenta shaded area), which is too slow to enrich a radius of $212.8h^{-1}$ kpc. However, this model is relevant for a single velocity shell and does not account for the full range of velocities observed in high-resolution spectra of the absorbing gas on $z \sim 2$ –3 star-forming galaxies.

Cosmological simulations that reproduce observables

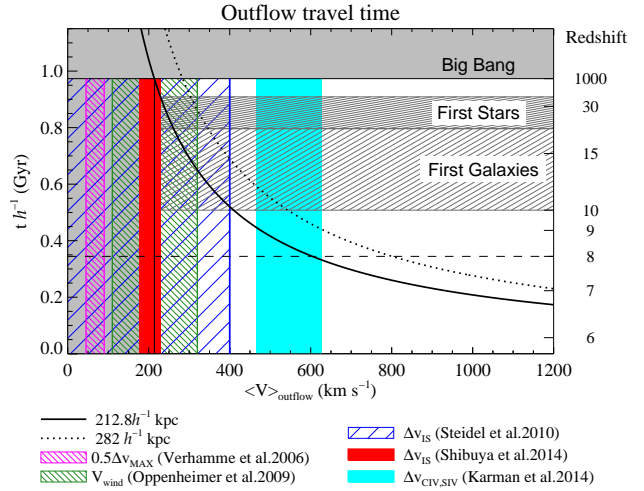


Figure 24. Travel time versus mean outflow velocity. The solid line and the dotted line indicate the time required to travel $212.8h^{-1}$ and $282h^{-1}$ physical kpc, respectively. The grey horizontal areas indicate the Big Bang, the time of formation of the first mini-halos to form stars, and the time of formation of the first galaxies. Vertical colour-coded regions represent observed and predicted outflow speeds from the literature.

like the comoving density of CIV ions in the IGM and the luminosity function of galaxies suggest that, among intergalactic metals, CIV is one of the best tracer of diffuse IGM in the redshift range $z = 5$ –6 and predict that star-forming galaxies in $\lesssim 10^9 M_{\odot}$ haloes pollute the IGM for the first time and provide the flux to maintain the ionization level of the systems up to 200 physical kpc (Oppenheimer, Davé & Finlator 2009). Moreover, the work of Oppenheimer, Davé & Finlator (2009) suggests that CIV absorption systems with column densities in the range $10^{12} - 10^{14} \text{ cm}^{-2}$ are probably associated with galaxies of luminosities $L \leq L^*$. Their best outflow model predicts mean outflow velocities between 200–250 km s^{-1} with decreasing trend towards higher redshift. In particular at $z \sim 5.7$, their best-fitting model predicts outflows with $110 < V_{wind} < 320 \text{ km s}^{-1}$ ($\pm 1\sigma$ range, green hatched area in Figure 24). This range is consistent with observations at lower redshift (e.g. Steidel et al. 2010; Shibuya et al. 2014) and, considering that the impact parameter of the galaxy-CIV pair is larger than similar column density examples at $z \leq 3.5$, it would imply that enriched gas expelled during the first stages of galaxy formation was able to reach the diffuse IGM more easily than the outflowing gas from star-formation episodes at later times, when galaxies are more massive.

Steidel et al. (2010) report that LBGs at $2 < z < 3$ show low-ionization absorption blue-shifted from the galaxy rest-frame, with the centroid of the IS line profiles (the bulk of the outflowing material) reaching $|\Delta v_{IS}| \lesssim 400$ (dark blue hashed area). Figure 24 clearly shows that such a velocity range implies an early onset of the outflowing mechanism ($z \lesssim 10$) in the LAE. In the same work, the authors confirm that the velocity profile of the strongest IS lines can reach $|v_{max}| \sim 700$ –800 km s^{-1} , which suggest that lower column density gas could be moving at these high speeds (Figure 8 of Steidel et al. 2010). Therefore, if the LAE has similar out-

flows and the velocity remains constant along the outflows' path, then low column density gas could reach the region of the C IV system by the time of observation. However, it is important to note that their sample of LBGs contains massive star-forming galaxies ($M_{\text{DM}} \sim 9 \times 10^{11} M_{\odot}$) whose gas kinematics are probably different from LAE 103027+052419.

A better comparison sample is given by Shibuya et al. (2014) who study LAEs at $z \sim 2.2$ and measure the velocity of Ly α and IS lines with respect to nebular emission lines. From a sample of four LAEs, they find a mean blue-shift of $\langle \Delta v_{\text{IS}} \rangle = 204 \pm 27 \text{ km s}^{-1}$ (red filled area) which is comparable to LBGs and not enough to disperse metals out to $212.8 h^{-1} \text{ kpc}$ by $z \sim 5.724$. This analysis suggests that typical outflow velocities found among lower redshift LAEs and LBGs struggle to support the scenario of a recent outflow from LAE 103027+052419 as the chemical origin of the C IV absorbing gas. Hence, it seems possible that outflows are active from very early times in the life of a star-forming galaxy. This early onset of galactic outflow supports the pre-galactic enrichment scenario where a significant fraction of the metals in the IGM were produced during the time of formation of the first galaxies or before.

So far, the comparison has been made with outflowing cool gas traced by low-ionization species (e.g. C II, Si II). However, highly ionized gas traced by high-ionization absorption, like C IV and Si IV, usually has larger outflow speed. For example, Figure 24 shows the outflow velocity measured by Karman et al. (2014) from C IV and Si IV in one of the star-forming galaxies in their sample at $z = 2.5\text{--}3.5$ (cyan filled region), for which they estimate the stellar mass $M_{\star} = 9.29 \times 10^9 M_{\odot}$ and age = $1.43 \times 10^8 \text{ yr}$. Thus, if LAE 103027+052419 had a similar outflow velocity around $z \sim 8$, such a highly ionised galactic wind could have reached $212.8 h^{-1} \text{ physical kpc}$ by $z = 5.724$.

Considering that the details of the distribution of metals around high- z galaxies are not fully understood, it is not clear yet if the amount of high-velocity material would be enough to produce the level of absorption that is observed ($\log N_{\text{C IV}} = 14.52 \pm 0.08$). For this reason and because the system has the highest C IV column density know to date at $z > 5.5$, we have chosen the conservative approach to compare with the speed of the bulk of the outflowing material (mean speed). From this comparison, we conclude that low-speed outflows are less probable to have enriched the distances observed in our example whereas high-speed low-density gas could transport some C IV to $212.8 h^{-1} \text{ kpc}$ in a reasonable cosmological time. Another alternative is that the carbon was produced and distributed by a closer undetected dwarf galaxy.

10.3 Undetected dwarf galaxies

Finally, we consider the scenario in which the C IV system is produced by a dwarf satellite galaxy gravitationally bound to the LAE. Our photometric sample reaches a luminosity limit of $L_{\text{Ly}\alpha} \sim 0.5 L_{\text{Ly}\alpha}^{\star}$ (star formation rate of $5\text{--}10 M_{\odot} \text{ yr}^{-1}$ uncorrected for IGM and dust absorption), where $L_{\text{Ly}\alpha}^{\star} = 6.8 \times 10^{42} h^{-2} \text{ erg s}^{-1}$ at $z = 5.7$ (Ouchi et al. 2008). Assuming the luminosity function of Ouchi et al. (2008) and a uniform distribution of galaxies, the number of LAEs brighter than $0.5 L_{\text{Ly}\alpha}^{\star}$ expected inside a projected area of radius $\sim 212 h^{-1} \text{ physical kpc}$ and within

$\pm 500 \text{ km s}^{-1}$ from the C IV system is ~ 0.03 . Having detected one LAE implies very low chances of having a second bright galaxy in such a small volume. However, under the hierarchical formation scenario, galaxies grow by accretion of less massive haloes. For this reason, it is possible that smaller haloes hosting galaxies below $0.5 L_{\text{Ly}\alpha}^{\star}$ are falling into LAE 103027+052419. However, the predicted number of faint LAEs depends on the faint end slope of the luminosity function (α). For example, using $\alpha = -1.5$ (e.g. Ouchi et al. 2008) the number of LAEs expected in the range $0.01\text{--}0.5 L_{\text{Ly}\alpha}^{\star}$ is ~ 0.79 . Interestingly, recent measurements of the Ly α luminosity function at $z \sim 5.7$ indicate a steeper faint end with $-2.35 < \alpha < -1.95$ (1σ , Dressler et al. 2014). Using $\alpha = -2.1$ and the luminosity function from Dressler et al. (2014), the predicted number of LAEs with $L_{\text{Ly}\alpha} = 0.01\text{--}0.5 L_{\text{Ly}\alpha}^{\star}$ is 0.98 (i.e. ~ 1). In other words: the most recent estimate of the LAE luminosity function at $z \sim 5.7$ predicts at least one LAE in the range $0.01\text{--}0.5 L_{\text{Ly}\alpha}^{\star}$ that would lie within a radius $\sim 212 h^{-1} \text{ physical kpc}$ and $\pm 500 \text{ km s}^{-1}$ from the C IV system. As a result, it is possible that the source of C IV is a galaxy fainter than our detection limit and closer to the absorption than LAE 103027+052419. However, this question will remain open until deeper observations are available.

A related possibility is that a faint galaxy is aligned exactly with the background QSO and therefore outshone by the QSO's brightness. Given the peculiarly high incidence of C IV absorption systems in this line of sight where four C IV systems have been found in the redshift range $5.5 < z < 6$ (Ryan-Weber et al. 2009; Simcoe et al. 2011; D'Odorico et al. 2013), the probability of having four galaxies and one QSO highly aligned with the observer is negligible. Moreover, low ionization absorptions like O I and C II are typically found in lines of sight to QSOs that intercept a galaxy "disc", indicating cool gas capable of forming stars. In this case, the absence of low ionization lines is in conflict with this scenario.

In summary, the LAE-C IV system pair with an impact parameter of $212.8 h^{-1} \text{ physical kpc}$ at $z = 5.724 \pm 0.001$ reported in this work, is in marginal agreement with the expectations from Oppenheimer, Davé & Finlator (2009) that C IV absorption systems at this redshift can be found at $\sim 200 h^{-1} \text{ physical kpc}$ of the galaxy providing the ionizing flux (the ionization 'bubble' model). Nevertheless, typical outflow velocities cannot support the idea that the LAE is the chemical source of the absorbing gas, unless highly ionised outflows can reach velocities twice as fast (or more) as the cool gas. Hence, the results agree with the idea that C IV systems are tracing lower density (diffuse) highly ionized IGM. On one hand, the possibility that the carbon was processed and distributed by an undetected dwarf satellite galaxy cannot be ruled out, whereas the late-outflow scenario would require a particularly high outflow speed (e.g. $\sim 800\text{--}1000 \text{ km s}^{-1}$ from LAE 103027+052419) not yet seen among lower redshift galaxies in the mass range of LAEs. On the other hand, if the progenitor of the carbon is indeed LAE 103027+052419, assuming a typical average speed of lower redshift outflows, we find a time of production and distribution of metals which is in agreement with the expectations from a cosmic chemical enrichment during a pre-galactic stage of galaxy formation (i.e. $z \gtrsim 8$). Therefore, re-

ardless of the origin of the carbon, the results are more easily explained by the pre-galactic enrichment scenario.

11 SUMMARY AND CONCLUSIONS

Following our findings of an excess of LAE candidates in the projected environment of $z \sim 5.7$ C IV absorption systems reported in Paper I, this work presents the results from the spectroscopic campaign using the DEIMOS spectrograph on the Keck-II telescope for LAEs in the fields J1030+0524 and J1137+3549. The main results are:

- The broad-band colours of confirmed LAEs are in agreement with the predictions in Paper I from the spectrophotometry of LBGs with Ly α emission. We find that LAEs at $z \sim 5.7$ are not recovered by the i' -dropout criteria since most of them have $(i' - z') < 1.3$.

- The contamination level in the LAE sample based on the asymmetry of the line is 10–20 per cent. We find that contaminant sources are more common at fainter magnitudes (NBC IV > 25 mag). No evidence for AGN was found in the spectroscopic sample of LAEs, although the search is heavily limited by the abundance of sky emission lines.

- Four out of the five LAEs within $10h^{-1}$ projected comoving Mpc of the C IV line of sight in the field J1030+0524 have been spectroscopically observed. If the emission line is Ly α , three are within $\pm 500 \text{ km s}^{-1}$ from the high-column density C IV system. This would confirm an excess of LAEs, which would become more significant ($\Sigma/\langle\Sigma\rangle \sim 2.4$) considering the volume sampled by the narrow-band. However, two LAEs were observed with low resolution and short exposure times and, although we identify the wavelength of the emission line, we cannot accurately measure the asymmetry of the line. Therefore, we cannot secure their LAE nature and the confirmation of the excess of LAEs on large scales will remain open until better data is acquired.

- We find that the LAE sample of the field J1137+3549 is not centred at the redshift of the C IV system but at lower redshift, as a result of the NBC IV sensitivity. Therefore, we cannot test the idea that LAEs dominate the environment of this absorption because the sample of LAEs is too distant from the environment of the C IV system. However, the absence of C IV at the redshift of the LAE sample and the large transverse distance to the closest LAE, would easily be explained if all LAEs are able to produce C IV absorption systems. This does not imply that all C IV systems are produced by LAEs.

- The redshift of the closest LAE to the C IV line of sight in J1030+0524 (LAE 103027+052419) is $z_{\text{Ly}\alpha} = 5.724 \pm 0.001$. This galaxy is at $212.8h^{-1}$ physical kpc transverse from the C IV absorption system at $z_{\text{C IV,b}} = 5.7242 \pm 0.0001$. This galaxy-C IV absorption system pair is the highest redshift example known to date, and involves the highest column density absorption system at $z \geq 5.5$.

This work has shown that our LAE sample is comparable to other $z \sim 5.7$ LAE searches, since in many instances we compare our measurements with the $z \sim 5.7$ LAEs from SDF and find very good agreement. Although the tentative detection of a small excess of LAEs in the line of sight around the C IV system will require better data to be confirmed, the

current picture seems to support the idea that C IV systems inhabit the surroundings of LAEs.

In the field J1030+0524, spectroscopy revealed the closest galaxy to a C IV absorption system at $z > 5.5$. We compared the observed properties of this LAE with the rest of the sample, in order to explore possible scenarios for the existence of a galaxy-C IV absorption system pair at $z \sim 5.7$. The main results can be summarised as follows:

- The Ly α emission line of LAE 103027+052419 shows a clear asymmetry ($S_{w,10\%} = 11.5 \pm 1.9$), low rest-frame equivalent width ($EW_0 = 33_{-12}^{+15} \text{ \AA}$) and a velocity shift of the emission peak $\Delta v_{\text{MAX}} = 136 \pm 45 \text{ km s}^{-1}$. The shape of the galaxy in the z' -band image from HST seems elongated towards the background QSO.

- Agreement between our sample and the sample of LAEs from SDF is found in the EW_0 distribution and the trend for UV fainter galaxies to have larger EW_0 .

- Compared with the rest of the sample, LAE 103027+052419 has one of the lowest values of EW_0 and the highest values of Δv_{MAX} .

- The UV luminosity, Ly α profile, Δv_{MAX} and EW_0 of LAE 103027+052419 suggest that this galaxy is at (or near) the high mass end of the LAEs, might contain a large HI column density and is a good candidate to host an outflow.

- The temporal limits imposed by the Big Bang and the formation of the first stars imply that outflow velocities typically observed at lower redshift are inconsistent with the LAE as the chemical source of the absorbing gas, unless highly ionised gas is moving more than twice the speed of the cool gas. Even in this case, the time of production and dispersion of metals would agree with predictions from the pre-galactic enrichment scenario.

- The luminosity function of LAEs at $z \sim 5.7$ predicts at least one LAE below our detection limit and within $\sim 212h^{-1}$ physical kpc radius (projected) and $\pm 500 \text{ km s}^{-1}$ (line of sight) from the C IV system. Therefore, outflows from undetected galaxies cannot be ruled out as the chemical origin of the absorption system.

The confirmation that LAE 103027+052419 is at $212.8_{-0.4}^{+14} h^{-1}$ physical kpc from the C IV system demonstrates that galaxies can be detected in association with high column density highly ionized metal absorption systems shortly after the epoch of reionization. However, our analysis suggests that typical outflow velocities found among lower redshift LAEs and LBGs do not support the scenario of an outflow from LAE 103027+052419 as the chemical origin of the C IV absorbing gas. The main implication is that the time when an outflow should have departed from the LAE agrees with the expectations from the pre-galactic enrichment scenario. Finally, we cannot rule out the possibility that the carbon was produced and distributed by an undetected dwarf galaxy fainter than LAEs. However, we note the low likelihood of dwarf galaxies aligned with the background QSO being responsible for all the C IV systems reported in this particular line of sight. Both options point towards an early ($z \gtrsim 6$) production and distribution of metals, which supports the idea that a significant fraction of the metals in the IGM were injected during a pre-galactic stage of galaxy formation.

As shown in this work, the search for galaxies around metal systems at high- z requires deep broad-band and

narrow-band photometry, which must be followed-up by spectroscopy resulting in a two-year process. In addition, observations are limited to sources identified from the photometry and the fraction of the sky with spectroscopic coverage is minimal. This procedure is far from ideal but has been the only option available so far. The optimal approach to study metal absorption systems and their galaxy counterparts would be a deep blind spectroscopic search around the absorptions. As a result, this field of research will be significantly benefited by new generation integral field units like MUSE on the *Very Large Telescope*, which provides the field of view, wavelength coverage and sensitivity that enable a blind spectroscopic search for galaxies around multiple absorption systems in the same line of sight. Instruments like MUSE are crucial to understand the physical state of the gas around high- z galaxies and its evolution, which is strongly related to mechanisms of chemical enrichment of the CGM and IGM.

ACKNOWLEDGMENTS

We are extremely grateful to Kym-Vy Tran whose data contribution obtained in February 2014 has significantly enriched the scientific output of this work. Many thanks to Neil Crighton, Valentina D’Odorico and Thibault Garel for their comments and the interesting conversations that we had over this work. C.G.D. acknowledges the support from the Victorian Government through the Victorian International Research Scholarship program. E.R.W. acknowledges the support of Australian Research Council grant DP1095600. J.C. acknowledges the support of Australian Research Council grant FF130101219. Y.K. acknowledges the support from the Japan Society for the Promotion of Science (JSPS) through JSPS research fellowships for young scientists. Y.K. also acknowledges the support by JSPS KAKENHI Number 26800107. M.O. acknowledges the supports from World Premier International Research Center Initiative (WPI Initiative), MEXT, Japan, and KAKENHI (23244025) Grant-in-Aid for Scientific Research(A) through Japan Society for the Promotion of Science (JSPS).

REFERENCES

- Ahn, S. H., Lee, H. W., Lee, H. M., 2003, MNRAS, 340, 863
- Ando, M., Ohta, K., Iwata, I., Akiyama, M., Aoki, K., and Tamura, N. 2006, ApJ, 645, L9
- Adelberger, K., Steidel, C., Shapley, A., & Pettini, M. 2003, ApJ, 584, 45
- Adelberger, K. L., Shapley, A. E., Steidel, C. C., Pettini, M., Erb, D. K. & Reddy, N. A. 2005, ApJ, 629, 636
- Barkana, R., and Loeb, A. 2001, Physics Reports 349, 125
- Behrens, C., Dijkstra, M., and Niemeyer, J. C. 2014, A&A, 563, 77
- Becker, G. D., Sargent, W. L. W., Rauch, M. & Simcoe, R. 2006, ApJ, 640, 69
- Becker, G. D., Rauch, M. & Sargent, W. L. W. 2009, ApJ, 698, 1010
- Becker, G. D., Sargent, W. L. W., Rauch, M., & Calverley, A. P. 2011, ApJ, 735, 93
- Becker, G. D., Hewett, P. C., Worseck, G., and Prochaska, J. X. 2013, MNRAS, 430, 2067
- Bouché, N., Hohensee, W., Vargas, R., Kacprzak, G.G., Martin, C.L., Cooke, J., and Churchill, C. W. 2012, MNRAS, 426, 801
- Bouwens, R. J., Illingworth, G. D., Franx, M. & Ford, H. 2007, ApJ, 670, 928
- Bouwens, R. J., Illingworth, G.D., Oesch, P.A., Trenti, M., Labbe, I., Bradley, L., Carollo, M., van Dokkum, P.G., et al. 2014, arXiv:1403.4295, submitted to ApJ
- Bradshaw, E. J., Almaini, O., Hartley, W. G., Smith, K. T., Conselice, C. J., Dunlop, J. S., Simpson, C., Chuter, R. W., et al. 2013, MNRAS, 433, 194
- Brook, C. B., Stinson, G., Gibson, B. K., Ro?kar, R., Wadley, J., and Quinn, T. 2012, MNRAS, 419, 771
- Bromm, V., and Yoshida, N. 2011, ARAA, 49, 373
- Cai, Z.-Y., Lapi, A., Bressan, A., De Zotti, G., Negrello, M., and Danese, L. 2014, ApJ, 785, 65
- Cassata, P., et al. 2011, A&A, 525, 143
- Cen, R., Chisari, N. E. 2011, ApJ, 731, 11
- Chonis, T. S., Blanc, G. A., Hill, G. J., Adams, J. J., Finkelstein, S. L., Gebhardt, K., Kollmeier, J. A., Ciardullo, R., et al. 2013, ApJ, 775, 99
- Coil, A. L., Weiner, B.J., Holz, D.E., Cooper, M.C., Yan, R., and Aird, J. 2011, ApJ, 743, 46
- Cooper, M. C., Newman, J. A., Davis, M., Finkbeiner, D. P., and Gerke, B. F. 2012, ASCL, 03003
- Díaz, C. G., Ryan-Weber, E., Cooke, J., Pettini, M. & Madau, P. 2011, MNRAS, 418, 820
- Diaz, C. G., Koyama, Y., Ryan-Weber, E. V., Cooke, J., Ouchi, M., Shimasaku, K., and Nakata F. 2014, MNRAS, 442, 946 (Paper I)
- Dijkstra, M. and Wyithe, J. S. B. 2010, MNRAS, 408, 352
- Dijkstra, M., and Kramer, R. 2012, MNRAS, 424, 1672
- D’Odorico, V., Cupani, G., Cristiani, S., Maiolino, R., Molaro, P., Nonino, M., Centurión, M., et al. 2013, MNRAS, 435, 1198
- Dressler, A., Martin, C.L., Henry, A., Sawicki, M., & McCarthy, P. 2011, ApJ, 740, 71
- Dressler, A., Henry, A., Martin, C.L., Sawicki, M., McCarthy, P., & Villaneuva, E. 2014, ArXiv, 1412.0655
- Fan, X., Strauss, M.A., Becker, R.H., White, R.L., Gunn, J.E., Knapp, G.R., Richards, G.T., Schneider, D.P., Brinkmann, J., and Fukugita, M. 2006, AJ, 132, 117
- Ferrara, A., & Loeb, A. 2013, MNRAS, 431, 2826
- Finkelstein, S. L., Hill, G.J., Gebhardt, K., Adams, J., Blanc, G.A., Papovich, C., Ciardullo, R., Drory, N., et al. 2011, ApJ, 729, 140
- Finkelstein, S. L., et al. 2012, ApJ, 758, 93.
- Fontanot, F., Cristiani, S., and Vanzella, E. 2012, MNRAS, 425, 1413
- Fontanot, F., Cristiani, S., Pfrommer, C., Cupani, G., & Vanzella, E. 2014, MNRAS, 438, 2097
- Gao, L., Yoshida, N., Abel, T., Frenk, C.S., Jenkins, A., and Springel, V. 2007, MNRAS, 378, 449
- Garel, T., Blaizot, J., Guiderdoni, B., Schaerer, D., Verhamme, A., and Hayes, M. 2012, MNRAS, 422, 310
- González, V., Labbé, I., Bouwens, R.J., Illingworth, G., Franx, M., & Kriek, M. 2011, ApJL, 735, L34
- Greif, T. H., Glover, S. C. O., Bromm, V., and Klessen, R.S. 2010, ApJ, 716, 510
- Hansen, M., and Oh, S. P. 2006, MNRAS, 367, 979

- Hashimoto, T., Ouchi, M., Shimasaku, K., Ono, Y., Nakajima, K., Rauch, M., Lee, J., and Okamura, S. 2013, *ApJ*, 775, 140
- Hopkins, P. F., Quataert, E., and Murray, N. 2012, *MNRAS*, 421, 3522
- Hu, E. M., Cowie, L. L., Capak, P., McMahon, R. G., Hayashino, T., & Komiyama, Y. 2004, *ApJ*, 127, 563
- Hu, E., Cowie, L., Barger, A., Capak, P., Kakazu, Y., & Trouille, L. 2010, *ApJ*, 725, 394
- Jeeson-Daniel, A., Ciardi, B., Maio, U., Pierleoni, M., Djikstra, M., and Maselli, A. 2012, *MNRAS*, 424, 2193
- Jensen, H., Laursen, P., Mellema, G., Iliev, I., Sommer-Larsen, J. & Shapiro, P. 2013, *MNRAS*, 428, 1366
- Jones, T., Stark, D., & Ellis, R. 2012, *ApJ*, 751, 51
- Karman, W., Caputi, K.I., Trager, S.C., Almaini, O., and Cirasuolo, M. 2014, *A&A*, 565, 5.
- Kashikawa, N. et al. 2006, *ApJ*, 648, 7
- Kashikawa, N., Shimasaku, K., Matsuda, Y., Egami, E., Jiang, L., Nagao, T., Ouchi, M., Malkan, M.A., Hattori, T., Ota, K., et al. 2011, *ApJ*, 734, 119
- Loeb, A. 2010, *How Did the First Stars and Galaxies Form?*, Princeton University Press.
- Ly, C., Malkan, M.A., Kashikawa, N., Shimasaku, K., Doi, M., Nagao, T., Iye, M., Kodama, T., Morokuma, T., and Motohara, K. 2007, *ApJ*, 657, 738
- Madau, P., Pozzetti, L., and Dickinson, M. 1998, *ApJ*, 498, 106
- Madau, P., Ferrara, A., and Rees, M.J. 2001, *ApJ*, 555, 92
- Malhotra, S., & Rhoads, J. E. 2002, *ApJL*, 565, L71
- Martin, C. L. 2005, *ApJ*, 621, 227
- Martin, C. L., Scannapieco, E., Ellison, S. L., Hennawi, J. F., Djorgovski, S. G., & Fournier, A. P. 2010, *ApJ*, 721, 174
- Martin, C.L., Shapley, A.E., Coil, A.L., Kornei, K.A., Bundy, K., Weiner, B.J., Noeske, K.G., and Schiminovich, D. 2012, *ApJ*, 760, 127
- McLinden, E.M., Finkelstein, S.L., Rhoads, J.E., Malhotra, S., Hibon, P., Richardson, M.L.A., Cresci, G., Quirrenbach, A., et al. 2011, *ApJ*, 730, 136
- McLinden, E.M., Rhoads, J.E., Malhotra, S., Finkelstein, S.L., Richardson, M.L.A., Smith, B., Tilvi, V.S., 2014, *MNRAS*, 439, 446
- McLure, R. J., et al. 2011, *MNRAS*, 418, 2074
- Murray, N., Ménard, B., and Thompson, T.A. 2011, *ApJ*, 735, 66
- Newman, J. A., Cooper, M. C., Davis, M., Faber, S. M., Coil, A. L., Guhathakurta, P., Koo, D. C., Phillips, A. C., Conroy, C., Dutton, A. A., et al. 2013, *ApJS*, 208, 5
- Oesch, P. A., Bouwens, R.J., Illingworth, G.D., Labb, I., Smit, R., Franx, M., van Dokkum, P.G., Momcheva, I., 2014, *ApJ*, 786, 108
- Oppenheimer, B. D. & Davé, R. 2006, *MNRAS*, 373, 1265
- Oppenheimer, B. D. & Davé, R. 2008, *MNRAS*, 387, 577
- Oppenheimer, B. D., Davé, R. & Finlator, K. 2009, *MNRAS*, 396, 729
- Orsi, A., Lacey, C. G., and Baugh, C. M. 2012, *MNRAS*, 425, 87
- Osterbrock, D., E., Fulbright, J., P., Martel, A., R., Keane, M., J., Trager, S., C., and Basri, G. 1996, *PASP*, 108, 277
- Ouchi, M. et al. 2004, *ApJ*, 611, 685
- Ouchi, M. et al. 2005, *ApJL*, 620, L1
- Ouchi, M., Shimasaku, K., Akiyama, M., Simpson, C., Saito, T., Ueda, Y., Furusawa, H., Sekiguchi, K., Yamada, T., Kodama, T., et al. 2008, *ApJ*, 176, 301
- Ouchi, M. et al. 2010, *ApJ*, 723, 869
- Pallottini, A., Ferrara, A., Gallerani, S., Salvadori, S., and D’Odorico, V. 2014, *MNRAS*, 440, 2498
- Pettini, M., Madau, P., Bolte, M., Prochaska, J. X., Ellison, S. L. & Fan, X. 2003, *ApJ*, 594, 695
- Porciani, C. & Madau, P. 2005, *ApJ*, 625, L43
- Rhoads, J. E., Dey, A., Malhotra, S., Stern, D., Spinrad, H., Jannuzi, B. T., Dawson, S., Brown, M. J. I., and Landes, E. 2003, *AJ*, 125, 1006
- Rupke, D. S., Veilleux, S. & Sanders, D. B. 2005, *ApJS*, 160, 115
- Ryan-Weber, E. V., Pettini, M., Madau, P. & Zych, B. J. 2009, *MNRAS*, 395, 1476
- Schmidt, K. B., Treu, T., Trenti, M., Bradley, L. D., Kelly, B. C., Oesch, P. A., Holwerda, B. W., Shull, J. M., and Stiavelli, M. 2014, *ApJ*, 786, 57.
- Shapley, A. E., Steidel, C. C., Pettini, M., & Adelberger, K. L. 2003, *ApJ*, 588, 65
- Shen, S., Madau, P., Aguirre, A., Guedes, J., Mayer, L., and Wadsley, J. 2012, *ApJ*, 760, 50
- Shibuya, T., Ouchi, M., Nakajima, K., Hashimoto, T., Ono, Y., Rauch, M., Gauthier, J.-R., Shimasaku, K., et al. 2014, *ApJ*, 788, 74
- Shimasaku, K., Kashikawa, N., Doi, M., Ly, C., Malkan, M.A., Matsuda, Y., Ouchi, M., Hayashino, T., Iye, M., Motohara, K., et al. 2006, *PASJ*, 58, 313
- Simcoe R. A. 2006, *ApJ*, 653, 977
- Simcoe R. A., et al. 2011, *ApJ*, 743, 21
- Songaila, A. 2001, *ApJ*, 561, L153
- Stanway, E., et al. 2007, *MNRAS*, 376, 727
- Steidel, C. C., Erb, D. K., Shapley, A. E., Pettini, M., Reddy, N., Bogosavljević, M., Rudie, G. C. and Rakic, O. 2010, *ApJ*, 717, 289
- Tescari, E., Viel, M., D’Odorico, V., Cristiani, S., Calura, F., Borgani, S., & Tornatore, L. 2011, *MNRAS*, 411, 826
- Vanzella, E., et al. 2009, *ApJ*, 695, 1163
- Verhamme, A., Schaerer, D., & Maselli, A., 2006, *A&A*, 460, 397
- Verhamme, A., Schaerer, D., Atek, H., and Tapken, C. 2008, *A&A*, 491, 89
- Verhamme, A., Orlitova, I., Schaerer, D., and Hayes, M. 2014, *ArXiv*, 1404.2958, submitted to *A&A*
- Wang, J.X., Rhoads, J.E., Malhotra, S., Dawson, S., Stern, D., Dey, A., Heckman, T.M., Norman, C.A., and Spinrad, H. 2004, *ApJL*, 608, L21
- Weiner, B. J., et al. 2009, *ApJ*, 692, 187
- Yoshida, N., Abel, T., Hernquist, L., and Sugiyama, N. 2003, *ApJ*, 592, 645
- Zheng, Z., Cen, R., Trac, H., and Miralda-Escud, J. 2010, *ApJ*, 716, 574
- Zheng, Z. Y., Wang, J.X., Finkelstein, S.L., Malhotra, S., Rhoads, J.E., and Finkelstein, K.D. 2010, *ApJ*, 718, 52
- Zheng, Z.-Y., Wang, J.-X., Malhotra, S., Rhoads, J. E., Finkelstein, S. L., and Finkelstein, K. 2014, *MNRAS*, 439, 1101

Table A1. LAEs in the field J1030+0524. The double line separates LAEs observed with the 600ZD grating, which are not selected by their weighted skewness because the emission lines are barely detected, but are presented for completeness.

| ID | Grating | RA (J2000) | Dec. (J2000) | z_{MAX} | z_{BLUE} | $S_{w,10\%}$ | $\text{EW}_{0,\text{Spec.}}$ (Å) | $\text{EW}_{0,\text{Phot.}}$ (Å) | Δv_{MAX} (km s $^{-1}$) |
|----|---------|---------------|-----------------|------------------|-------------------|--------------|-------------------------------------|-------------------------------------|--|
| 1 | 830G | 10:30:21.535 | +5:32:56.33 | 5.671±0.001 | 5.663±0.001 | 16.0±1.1 | >35 | 203 $^{+97}_{-70}$ | 344±46 |
| 2 | 830G | 10:30:21.442 | +5:36:49.99 | 5.661±0.001 | 5.658±0.001 | 14.8±1.0 | 52±36 | 46 $^{+17}_{-13}$ | 137±46 |
| 3 | 830G | 10:30:36.902 | +5:17:08.33 | 5.704±0.001 | 5.701±0.001 | 11.9±0.9 | 175±159 | 84 $^{+60}_{-35}$ | 119±46 |
| 4 | 830G | 10:30:27.677 | +5:24:19.82 | 5.727±0.001 | 5.724±0.001 | 11.5±1.9 | 40±31 | 33 $^{+15}_{-12}$ | 136±46 |
| 5 | 830G | 10:29:49.853 | +5:24:37.91 | 5.737±0.001 | 5.734±0.001 | 10.1±1.2 | >8 | 153 $^{+142}_{-71}$ | 102±46 |
| 6 | 830G | 10:30:06.358 | +5:17:42.10 | 5.749±0.001 | 5.747±0.001 | 8.70±1.2 | 71±61 | 151 $^{+138}_{-75}$ | 119±46 |
| 7 | 830G | 10:29:56.062 | +5:21:28.64 | 5.690±0.001 | 5.689±0.001 | 8.50±2.8 | >5 | 61 $^{+68}_{-34}$ | 51±46 |
| 8 | 830G | 10:29:49.994 | +5:24:17.49 | 5.740±0.001 | 5.738±0.001 | 8.10±1.0 | >25 | 178 $^{+142}_{-83}$ | 102±46 |
| 9 | 830G | 10:30:15.722 | +5:34:59.51 | 5.712±0.001 | 5.709±0.001 | 7.40±1.7 | 28±22 | 38 $^{+21}_{-15}$ | 155±46 |
| 10 | 830G | 10:30:32.050 | +5:19:28.76 | 5.702±0.001 | 5.701±0.001 | 6.20±1.9 | >2 | >297 | 52±46 |
| 11 | 830G | 10:29:56.844 | +5:21:36.72 | 5.692±0.001 | 5.689±0.001 | 6.00±2.0 | 22±19 | 69 $^{+47}_{-26}$ | 120±46 |
| 12 | 830G | 10:30:15.689 | +5:15:50.90 | 5.684±0.001 | 5.682±0.001 | 5.90±0.7 | 120±104 | 77 $^{+31}_{-25}$ | 69±46 |
| 13 | 830G | 10:30:37.937 | +5:23:04.58 | 5.688±0.001 | 5.686±0.001 | 4.00±1.8 | 15±11 | 66 $^{+80}_{-36}$ | 103±46 |
| 14 | 830G | 10:29:51.226 | +5:20:57.26 | 5.678±0.001 | 5.676±0.001 | 3.70±1.6 | >8 | 90 $^{+100}_{-45}$ | 103.0±46 |
| 15 | 830G | 10:29:51.562 | +5:28:05.61 | 5.697±0.001 | 5.695±0.001 | 3.20±1.9 | 14±12 | 44 $^{+28}_{-19}$ | 85±46 |
| 16 | 830G | 10:30:40.385 | +5:16:18.11 | 5.699±0.001 | 5.698±0.001 | 3.00±1.2 | >4 | >133 | 51±46 |
| 17 | 830G | 10:30:26.911 | +5:37:01.61 | 5.656±0.001 | 5.649±0.001 | 1.10±1.1 | 27±20 | 38 $^{+56}_{-31}$ | 291±46 |
| 18 | 830G | 10:30:15.727 | +5:27:37.67 | 5.726±0.001 | 5.723±0.001 | -1.4±1.9 | >3 | >149 | 119±46 |
| 19 | 600ZD | 10:30:33.41 | +5:23:41.8 | 5.728±0.001 | 5.726±0.001 | 3.20±4.3 | >3 | 60 $^{+18}_{-13}$ | 71±64 |
| 20 | 600ZD | 10:30:40.80 | +5:27:17.4 | 5.717±0.001 | 5.715±0.001 | 0.00±5.2 | 52±50 | 57 $^{+17}_{-14}$ | 94±64 |
| 21 | 600ZD | 10:29:59.36 | +5:21:55.9 | 5.738±0.001 | 5.736±0.001 | -1.7±5.4 | >1 | >142 | 94±64 |

SPECTROSCOPIC SAMPLE OF $z \sim 5.7$ LAES.

This Appendix contains tables with measurements of spectroscopic quantities and other estimates for the sample of LAE candidates observed with DEIMOS. A summary of their photometry is also presented for completeness. The objects are sorted by decreasing weighted skewness $S_{w,10\%}$. The dashed line separates objects with $S_{w,10\%} < 3$, which do not reach the asymmetry condition and are considered contaminants. However, all quantities reported are estimated assuming that the emission line is Ly α .

The columns of Tables A1 and A3 contain: (1) ID number that follows the sorting criteria of decreasing $S_{w,10\%}$; (2) name of the grating used in the spectroscopic observations; (3) right ascension and (4) declination (FK5, J2000.0); (5) redshift measured at the maximum of the line profile; (6) redshift measured at the bluest pixel of the line profile (as described in Section 5); (7) weighted skewness $S_{w,10\%}$ measured as described in Section 3.2; (8) equivalent width measured from the photometry and (9) from the spectra, as described in Section 8.1; (10) velocity shift of the maximum of the line profile with respect to z_{BLUE} .

The columns of Tables A2 and A4 contain: (1) ID number; (2) absolute magnitude and (3) luminosity in the rest-frame ultraviolet ($\lambda_0 \sim 1350 \text{Å}$); (4) star formation rate (SFR) estimated from the ultraviolet luminosity via $L_{\text{UV}} = 8.0 \times 10^{27} \text{SFR}_{\text{UV}} \frac{(\text{erg s}^{-1} \text{Hz}^{-1})}{(M_{\odot} \text{yr}^{-1})}$ (Madau, Pozzetti & Dickinson 1998); (5), (6), (7) and (8) the aperture photometry in the R $_c$, i' , z' and NBC IV bands, respectively; and (9) present the NB excess ($i' - \text{NBC IV}$).

Table A2. LAEs in the field J1030+0524.

| ID | M_{UV} (mag) | L_{UV} ($\times 10^{28}$ erg s $^{-1}$ Hz $^{-1}$) | SFR_{UV} (M_{\odot} yr $^{-1}$) | R_c (2 arcsec) | i' (2 arcsec) | z' (2 arcsec) | NB_{CIV} (2 arcsec) | $(i'-NB_{CIV})$ (2 arcsec) |
|----|-------------------|---|--|---------------------|--------------------|--------------------|--------------------------|-------------------------------|
| 1 | -20.7 \pm 0.5 | 9.1 \pm 4.1 | 11.4 \pm 5.1 | \gtrsim 28.35 | 26.24 \pm 0.30 | 25.92 \pm 0.53 | 24.19 \pm 0.05 | 2.0 |
| 2 | -21.7 \pm 0.2 | 21.0 \pm 4.7 | 26.2 \pm 5.9 | \gtrsim 28.35 | 25.95 \pm 0.24 | 24.92 \pm 0.25 | 24.44 \pm 0.08 | 1.4 |
| 3 | -20.6 \pm 0.7 | 9.20 \pm 5.5 | 11.5 \pm 6.9 | \gtrsim 28.35 | 26.85 \pm 0.486 | 26.40 \pm 0.75 | 24.35 \pm 0.05 | 2.6 |
| 4 | -20.7 \pm 0.5 | 9.50 \pm 4.2 | 11.9 \pm 5.2 | \gtrsim 28.35 | \gtrsim 28.04 | 25.89 \pm 0.52 | 25.11 \pm 0.15 | \gtrsim 3.0 |
| 5 | -19.9 \pm 0.9 | 5.3 \pm 3.8 | 6.6 \pm 4.7 | \gtrsim 28.35 | 26.88 \pm 0.50 | 26.77 \pm 0.95 | 24.58 \pm 0.09 | 2.1 |
| 6 | -19.7 \pm 1.0 | 4.8 \pm 3.5 | 6.7 \pm 4.4 | \gtrsim 28.35 | \gtrsim 28.04 | 26.9 \pm 1.0 | 25.07 \pm 0.13 | \gtrsim 3.0 |
| 7 | -19.8 \pm 1.0 | 5.2 \pm 3.7 | 6.5 \pm 4.6 | \gtrsim 28.35 | 27.24 \pm 0.642 | 26.79 \pm 0.96 | 25.47 \pm 0.21 | 1.9 |
| 8 | -20.0 \pm 0.9 | 5.7 \pm 3.800 | 7.1 \pm 4.7 | \gtrsim 28.35 | 27.09 \pm 0.58 | 26.66 \pm 0.88 | 24.42 \pm 0.07 | 2.6 |
| 9 | -20.6 \pm 0.6 | 8.5 \pm 4.2 | 10.6 \pm 5.2 | \gtrsim 28.35 | 27.27 \pm 0.65 | 26.03 \pm 0.58 | 25.03 \pm 0.12 | 2.1 |
| 10 | >-19.1 | <2 | <2.5 | \gtrsim 28.35 | 27.42 \pm 0.72 | \gtrsim 27.49 | 25.55 \pm 0.21 | 1.8 |
| 11 | -20.4 \pm 0.6 | 7.6 \pm 4.1 | 9.5 \pm 5.1 | \gtrsim 28.35 | 26.90 \pm 0.50 | 26.19 \pm 0.65 | 24.80 \pm 0.12 | 1.6 |
| 12 | -20.9 \pm 0.4 | 11.0 \pm 4.3 | 13.7 \pm 5.3 | \gtrsim 28.35 | 25.90 \pm 0.23 | 25.69 \pm 0.45 | 24.36 \pm 0.07 | 1.6 |
| 13 | -19.7 \pm 1.0 | 4.7 \pm 3.4 | 5.9 \pm 4.2 | \gtrsim 28.35 | \gtrsim 28.04 | 26.9 \pm 1.0 | 25.61 \pm 0.18 | \gtrsim 2.3 |
| 14 | -19.9 \pm 0.9 | 5.4 \pm 3.7 | 6.7 \pm 4.6 | \gtrsim 28.35 | 27.01 \pm 0.54 | 26.72 \pm 0.92 | 25.29 \pm 0.16 | 1.8 |
| 15 | -20.4 \pm 0.6 | 7.7 \pm 4.1 | 9.6 \pm 5.1 | \gtrsim 28.35 | 27.37 \pm 0.70 | 26.17 \pm 0.64 | 25.13 \pm 0.20 | 2.2 |
| 16 | >-19.1 | <1.9 | <2.4 | \gtrsim 28.35 | \gtrsim 28.04 | \gtrsim 27.49 | 25.42 \pm 0.17 | \gtrsim 2.7 |
| 17 | -20.6 \pm 0.6 | 8.5 \pm 4.1 | 10.6 \pm 5.1 | \gtrsim 28.35 | 27.101 \pm 0.58 | 26.01 \pm 0.57 | 25.79 \pm 0.21 | 1.4 |
| 18 | >-19.1 | <1.9 | <2.4 | \gtrsim 28.35 | \gtrsim 28.04 | \gtrsim 27.49 | 25.24 \pm 0.13 | \gtrsim 2.6 |
| 19 | -21.2 \pm 0.4 | 13.6 \pm 4.5 | 17.0 \pm 5.6 | 27.67 \pm 0.62 | 26.36 \pm 0.33 | 25.44 \pm 0.37 | 24.12 \pm 0.08 | 1.7 |
| 20 | -21.2 \pm 0.4 | 14.3 \pm 4.6 | 17.9 \pm 5.7 | \gtrsim 28.35 | 26.49 \pm 0.37 | 25.38 \pm 0.36 | 24.02 \pm 0.08 | 2.2 |
| 21 | >-19.1 | <2.0 | <2.5 | \gtrsim 28.35 | \gtrsim 28.04 | \gtrsim 27.49 | 25.49 \pm 0.16 | 2.5 |

Table A3. Same as Table A1 for LAEs in the field J1137+3549.

| ID | Grating | RA (J2000) | Dec. (J2000) | z_{MAX} | z_{BLUE} | $S_w, 10\%$ | $EW_{0, Spec.}$ (\AA) | $EW_{0, Phot.}$ (\AA) | Δv_{MAX} (km s $^{-1}$) |
|----|---------|---------------|-----------------|---------------------|-------------------|----------------|-------------------------------------|-------------------------------------|-------------------------------------|
| 1 | 830G | 11:36:37.373 | +35:58:31.63 | 5.686 \pm 0.001 | 5.683 \pm 0.001 | 19.9 \pm 1.5 | 176 \pm 158 | 54 $^{+17}_{-12}$ | 119 \pm 46 |
| 2 | 830G | 11:36:37.606 | +35:41:03.10 | 5.708 \pm 0.001 | 5.705 \pm 0.001 | 16.9 \pm 1.3 | 29 \pm 18 | 76 $^{+24}_{-19}$ | 136 \pm 46 |
| 3 | 600ZD | 11:37:58.70 | +35:56:44.3 | 5.695 \pm 0.001 | 5.690 \pm 0.001 | 16.3 \pm 2.5 | 34 \pm 22 | 109 $^{+61}_{-42}$ | 190 \pm 65 |
| 4 | 830G | 11:36:49.742 | +35:57:59.24 | 5.683 \pm 0.001 | 5.681 \pm 0.001 | 14.6 \pm 1.5 | >4 | 83 $^{+46}_{-32}$ | 86 \pm 46 |
| 5 | 830G | 11:36:39.089 | +35:43:46.44 | 5.715 \pm 0.001 | 5.713 \pm 0.001 | 13.7 \pm 0.5 | 62 \pm 41 | 61 $^{+17}_{-14}$ | 103 \pm 46 |
| 6 | 830G | 11:36:45.269 | +35:40:40.37 | 5.708 \pm 0.001 | 5.705 \pm 0.001 | 13.5 \pm 0.8 | >26 | >220 | 136 \pm 46 |
| 7 | 830G | 11:36:47.088 | +35:44:02.22 | 5.682 \pm 0.001 | 5.679 \pm 0.001 | 10.9 \pm 0.2 | 193 \pm 141 | 283 $^{+200}_{-117}$ | 120 \pm 46 |
| 8 | 830G | 11:37:18.602 | +35:53:00.41 | 5.707 \pm 0.001 | 5.704 \pm 0.001 | 10.2 \pm 0.6 | >34 | 111 $^{+87}_{-47}$ | 120 \pm 46 |
| 9 | 600ZD | 11:38:05.27 | +35:58:11.5 | 5.708 \pm 0.001 | 5.705 \pm 0.001 | 5.30 \pm 2.9 | >6 | 30 $^{+5}_{-3}$ | 118 \pm 64 |
| 10 | 830G | 11:37:01.306 | +35:49:17.42 | 5.696 \pm 0.001 | 5.694 \pm 0.001 | 3.00 \pm 0.6 | >13 | 168 $^{+210}_{-105}$ | 86 \pm 46 |
| 11 | 600ZD | 11:38:07.69 | +35:54:42.6 | 0.6370 \pm 0.0005 | - | -1.7 \pm 1.0 | - | - | - |
| 12 | 600ZD | 11:37:39.82 | +35:52:38.2 | 5.713 \pm 0.001 | 5.708 \pm 0.001 | -3.6 \pm 2.4 | >7 | 81 $^{+64}_{-35}$ | 237 \pm 64 |

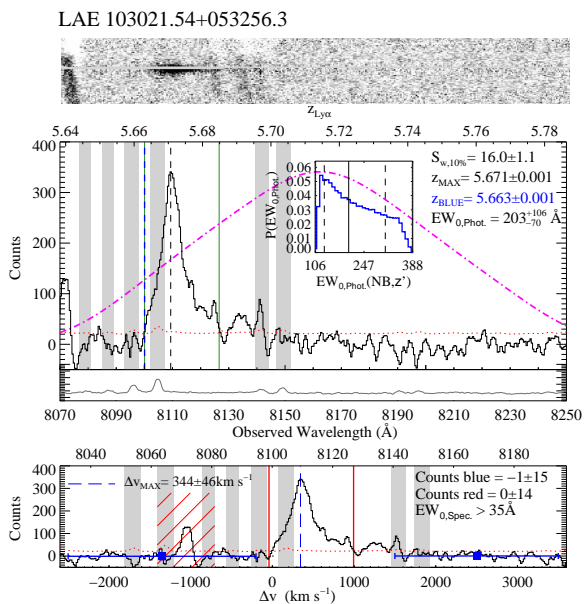
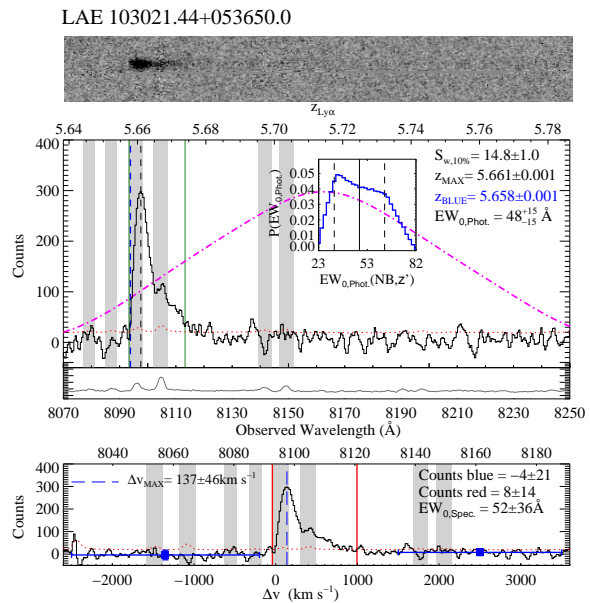
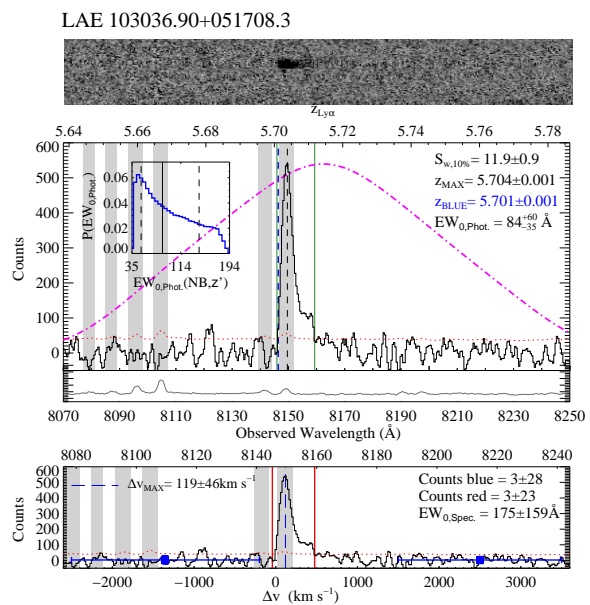
Table A4. Same as Table A2 for LAEs in the field J1137+3549.

| ID | M_{UV} (mag) | L_{UV} ($\times 10^{28}$ erg s $^{-1}$ Hz $^{-1}$) | SFR_{UV} (M_{\odot} yr $^{-1}$) | R_c (2 arcsec) | i' (2 arcsec) | z' (2 arcsec) | NB_{CIV} (2 arcsec) | $(i'-NB_{CIV})$ (2 arcsec) |
|----|-------------------|---|--|---------------------|--------------------|--------------------|--------------------------|-------------------------------|
| 1 | -21.5 \pm 0.3 | 18.1 \pm 4.9 | 22.6 \pm 6.1 | 27.26 \pm 0.56 | 26.02 \pm 0.30 | 25.10 \pm 0.30 | 24.04 \pm 0.17 | 1.5 |
| 2 | -21.1 \pm 0.4 | 13.0 \pm 4.7 | 16.2 \pm 5.9 | \gtrsim 28.04 | 26.77 \pm 0.54 | 25.50 \pm 0.41 | 23.89 \pm 0.11 | 2.4 |
| 3 | -20.5 \pm 0.6 | 8.10 \pm 4.3 | 10.1 \pm 5.4 | \gtrsim 28 | 26.46 \pm 0.43 | 26.12 \pm 0.65 | 24.33 \pm 0.12 | 2.1 |
| 4 | -20.6 \pm 0.6 | 9.0 \pm 4.4 | 11.2 \pm 5.5 | 27.64 \pm 0.73 | 26.37 \pm 0.40 | 25.96 \pm 0.58 | 24.58 \pm 0.13 | 1.7 |
| 5 | -21.3 \pm 0.3 | 15.4 \pm 4.8 | 19.2 \pm 6.0 | \gtrsim 28.04 | 25.95 \pm 0.28 | 25.30 \pm 0.35 | 23.88 \pm 0.06 | 2.1 |
| 6 | >-19.2 | <2.1 | <2.6 | \gtrsim 28.04 | \gtrsim 27.61 | \gtrsim 27.39 | 24.71 \pm 0.17 | \gtrsim 2.9 |
| 7 | -20.2 \pm 0.8 | 6.70 \pm 4.1 | 8.4 \pm 5.1 | \gtrsim 28.04 | 26.16 \pm 0.34 | 26.39 \pm 0.78 | 23.87 \pm 0.06 | 2.3 |
| 8 | -20.1 \pm 0.8 | 6.40 \pm 4.1 | 8.0 \pm 5.1 | \gtrsim 28.04 | \gtrsim 27.61 | \gtrsim 27.39 | 24.48 \pm 0.14 | \gtrsim 2.9 |
| 9 | -22.4 \pm 0.1 | 38.3 \pm 5.3 | 47.9 \pm 6.6 | 26.42 \pm 0.29 | 25.45 \pm 0.19 | 24.26 \pm 0.15 | 23.47 \pm 0.09 | 1.34 |
| 10 | -19.4 \pm 1.2 | 4.20 \pm 3.4 | 5.2 \pm 4.2 | \gtrsim 28.04 | \gtrsim 27.61 | 27.2 \pm 1.2 | 24.88 \pm 0.23 | \gtrsim 2.8 |
| 11 | - | - | - | \gtrsim 28.04 | 26.81 \pm 0.55 | 27.2 \pm 1.2 | 24.94 \pm 0.19 | 1.83 |
| 12 | -20.2 \pm 0.8 | 6.60 \pm 4.1 | 8.20 \pm 5.1 | \gtrsim 28.04 | \gtrsim 27.61 | 26.44 \pm 0.80 | 24.72 \pm 0.14 | 2.6 |

APPENDIX B: SPECTRA OF $z \sim 5.7$ LAES

This appendix presents individual LAE spectra observed with DEIMOS. Two objects have been omitted because they were presented previously. The first one is LAE 103027+052419 (object ID 4 in the field J1030+0524), which is presented in Figure 16, and the second one is the O III emitter at $z \sim 0.637$ (object ID 11 in the field J1137+3549) shown in Figure 6.

Each figure presents: the snapshot of the 2D slit spectrum in the wavelength range covered by the NBC IV filter, the 1D spectrum of the emission line, the equivalent width probability distribution obtained from the photometry and the 1D spectrum in velocity units with respect to the bluest pixel of the emission. In the middle panels (1D spectrum), the red dotted line indicates one standard deviation of the counts in the extraction box (1σ error), the magenta dot-dashed line is the scaled transmission curve of the NBC IV filter, the vertical dashed lines indicate the position of the maximum (black line) and the bluest pixel (blue line), and the grey shaded areas show the wavelength of the skylines where residuals can be large. The sky spectrum in an arbitrary scale is given for reference below each object spectrum. The weighted skewness is measured in the range contained by the vertical green solid lines that indicate $\lambda_{10\%,blue}$ and $\lambda_{10\%,red}$. In the inset panels ($P(EW_0)$), the solid line and the dashed lines indicate the central value of the distribution and the range enclosing a probability of 0.68. In the bottom panels (velocity units), the vertical solid lines indicate the wavelength range where the spectroscopic equivalent width was measured. The blue squares with error bars at each side of the emission lines show the mean counts level of the continuum, where the vertical error bars are the standard deviation of the flux in counts and the horizontal error bars are the wavelength range used to estimate the mean. At both sides of the emission, we avoided regions of significant skyline residuals (grey areas) and regions with high contamination from internally reflected light (red-hashed regions).


Figure B1. Field J1030+0524. ID 1

Figure B2. Field J1030+0524. ID 2

Figure B3. Field J1030+0524. ID 3

LAE 103015.72+053459.6

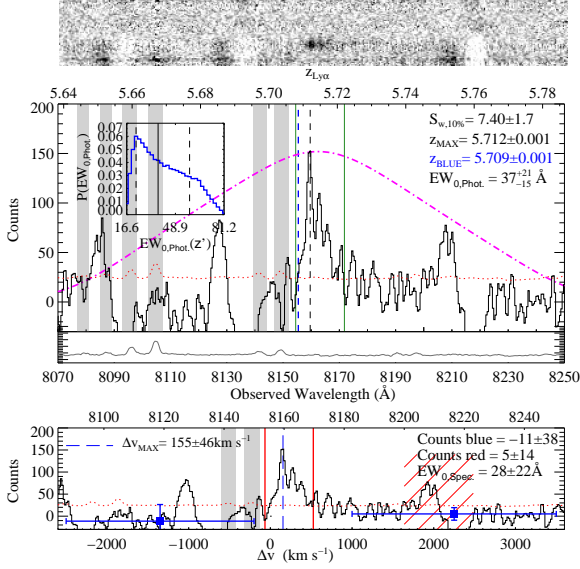


Figure B8. Field J1030+0524. ID 9

LAE 102956.85+052136.7

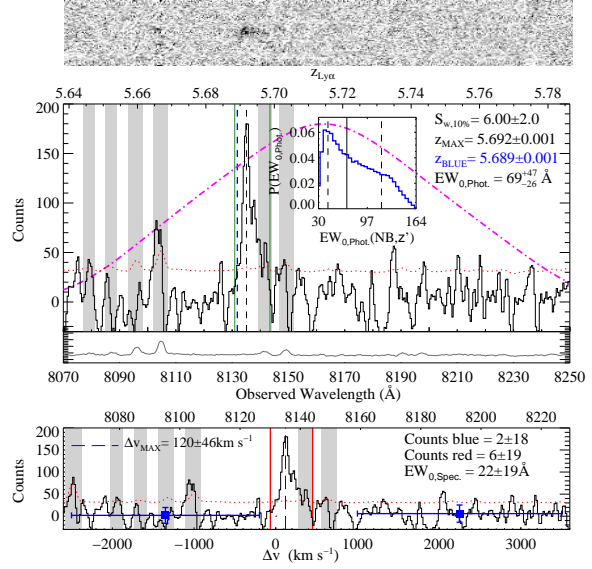


Figure B10. Field J1030+0524. ID 11

LAE 103032.05+051928.8

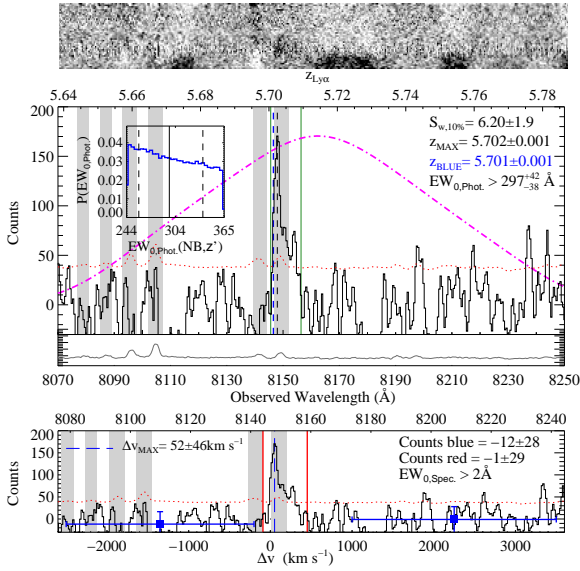


Figure B9. Field J1030+0524. ID 10

LAE 103015.69+051550.9

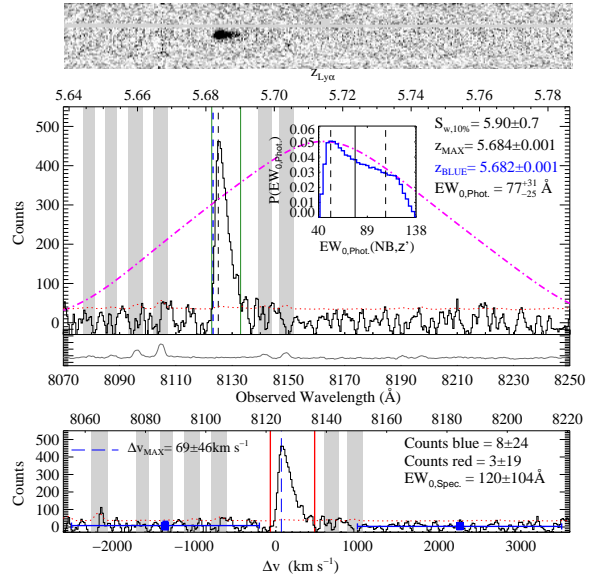


Figure B11. Field J1030+0524. ID 12

LAE 103037.94+052304.6

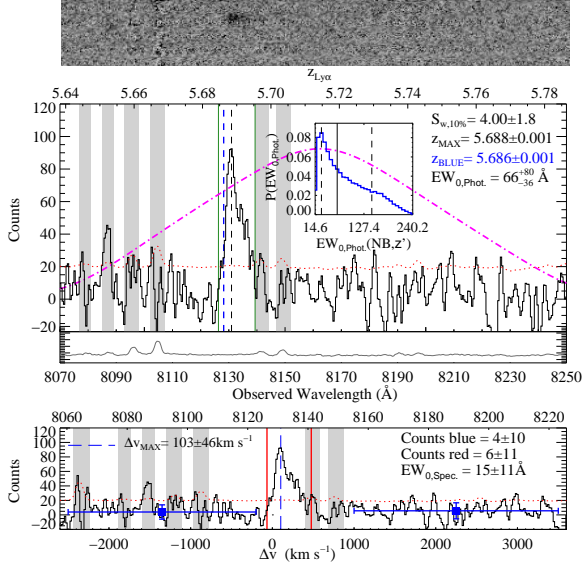


Figure B12. Field J1030+0524. ID 13

LAE 102951.56+052805.6

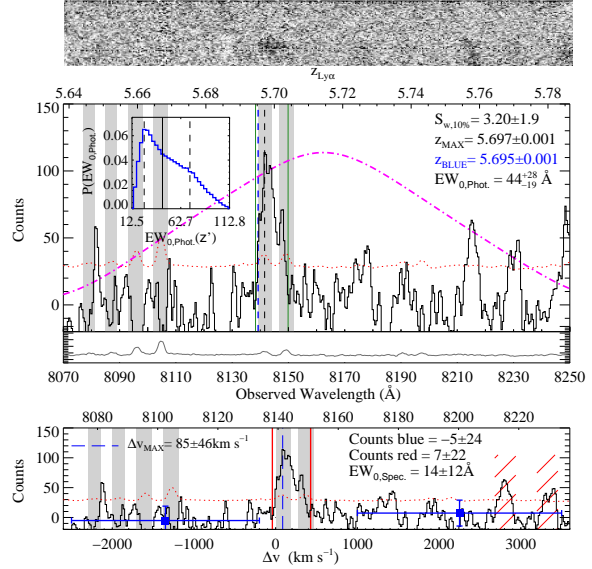


Figure B14. Field J1030+0524. ID 15

LAE 102951.23+052057.3

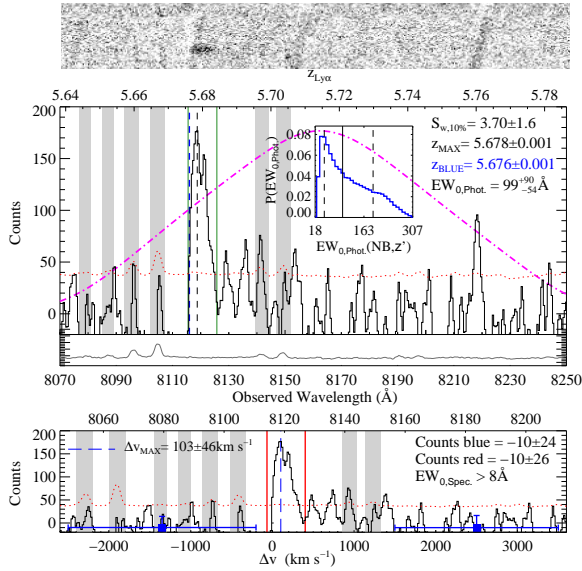


Figure B13. Field J1030+0524. ID14

LAE 103040.39+051618.1

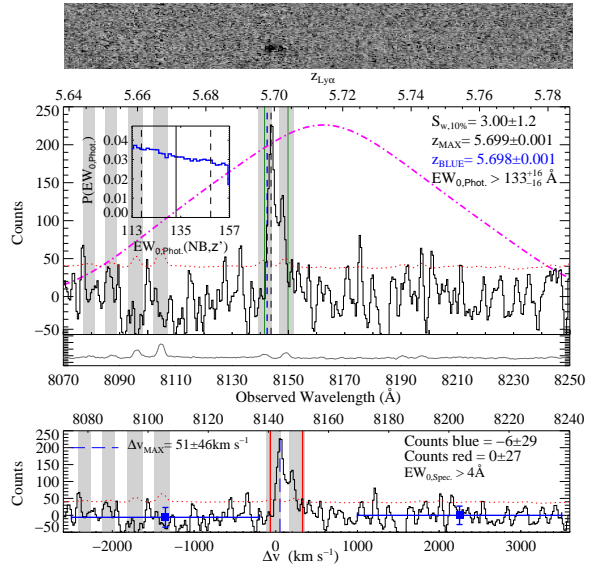


Figure B15. Field J1030+0524. ID 16

LAE 103026.91+053701.6

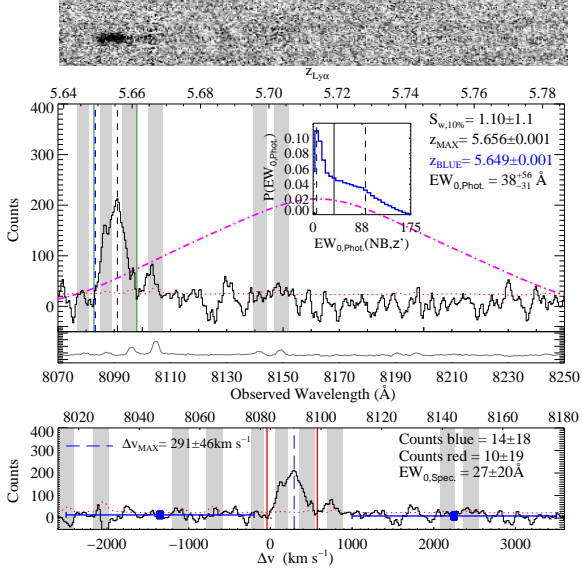


Figure B16. Field J1030+0524. ID 17

LAE 103033.41+052341.8 (600ZD)

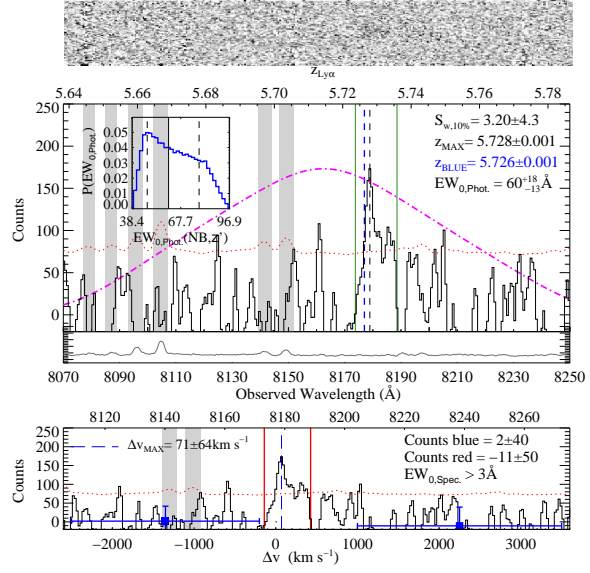


Figure B18. Field J1030+0524. ID 19

LAE 103015.73+052737.6

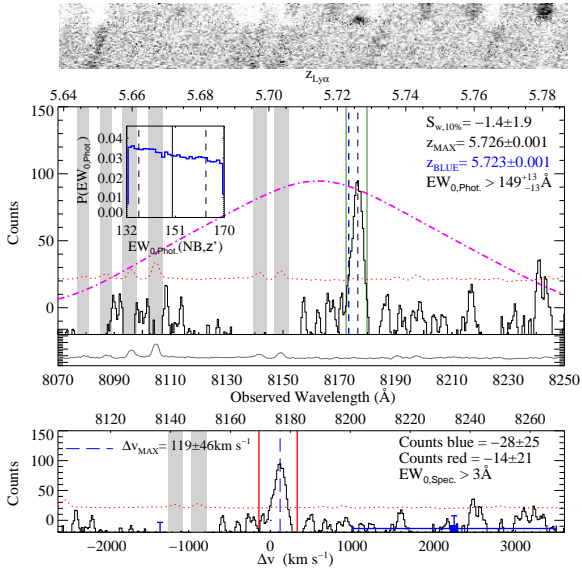


Figure B17. Field J1030+0524. ID 18

LAE 103040.8+052717.4 (600ZD)

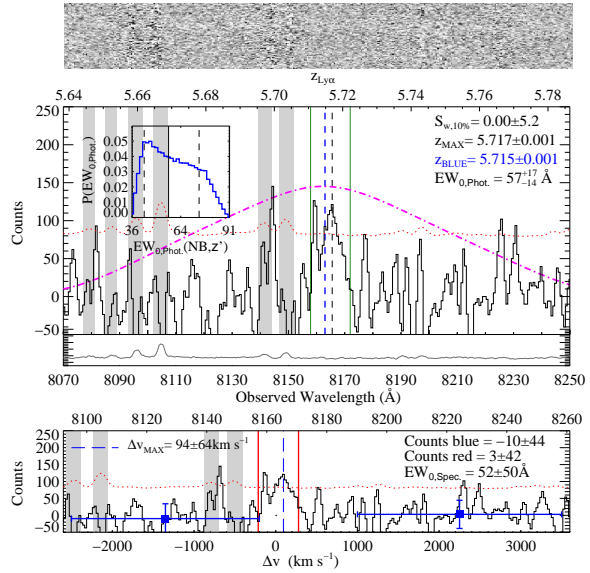


Figure B19. Field J1030+0524. ID 20

LAE 102959.36+052155.9 (600ZD)

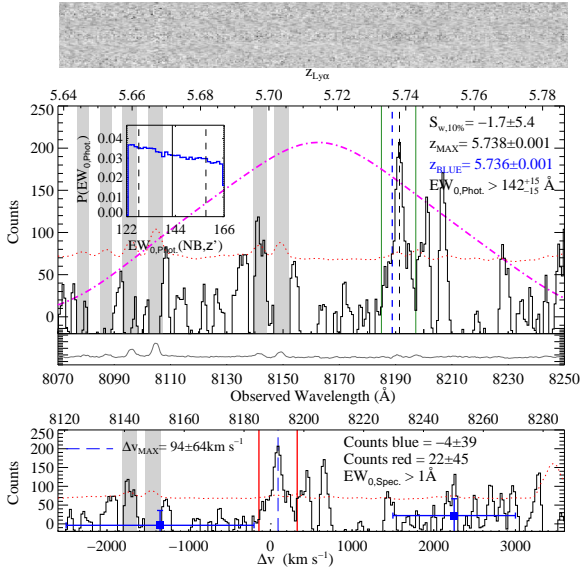


Figure B20. Field J1030+0524. ID 21

LAE 113637.61+354103.1

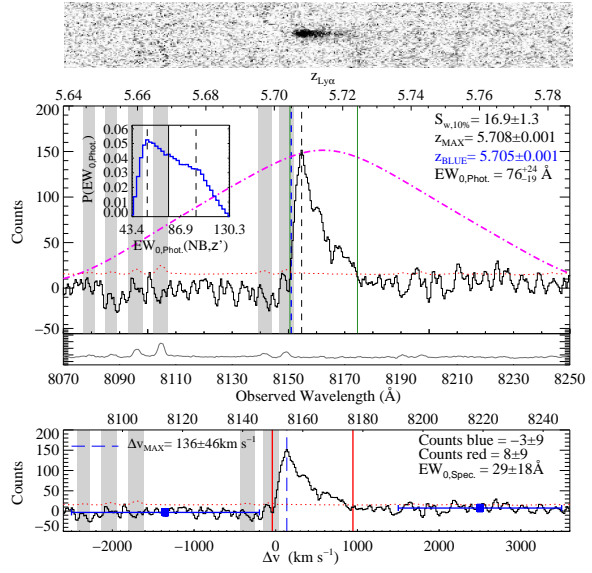


Figure B22. Field J1137+3549. ID 2

LAE 113637.38+355831.6

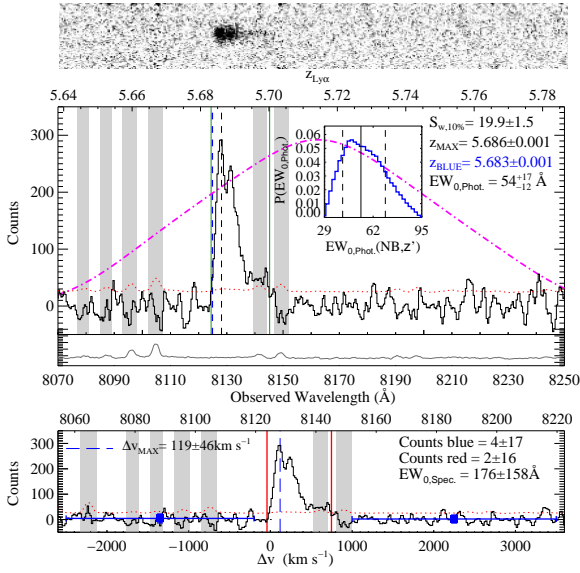


Figure B21. Field J1137+3549. ID 1

LAE 113758.70+355644.3 (600ZD)

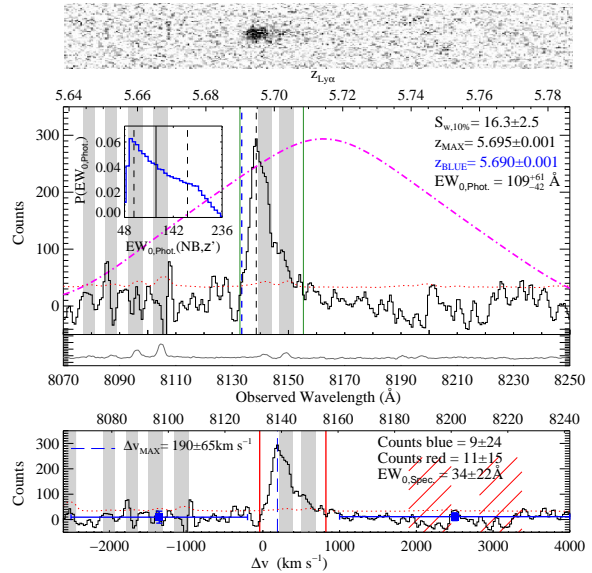


Figure B23. Field J1137+3549. ID 3

LAE 113649.74+355759.2

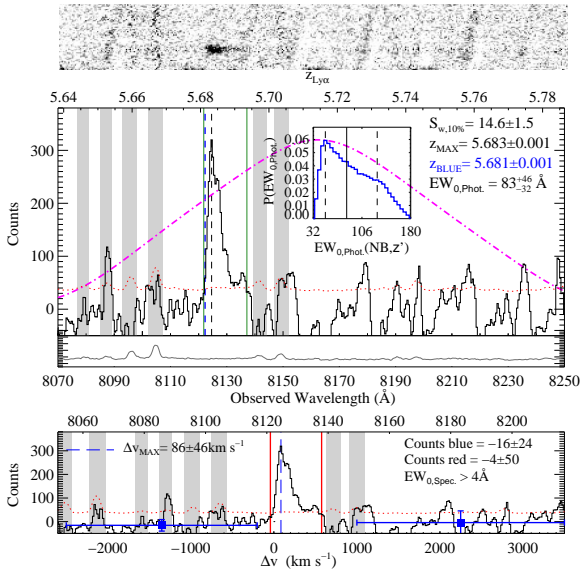


Figure B24. Field J1137+3549. ID 4

LAE 113645.27+354040.4

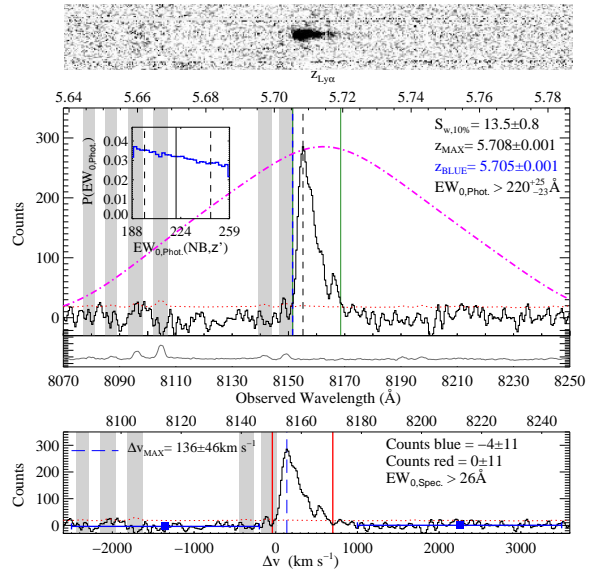


Figure B26. Field J1137+3549. ID 6

LAE 113639.09+354346.4

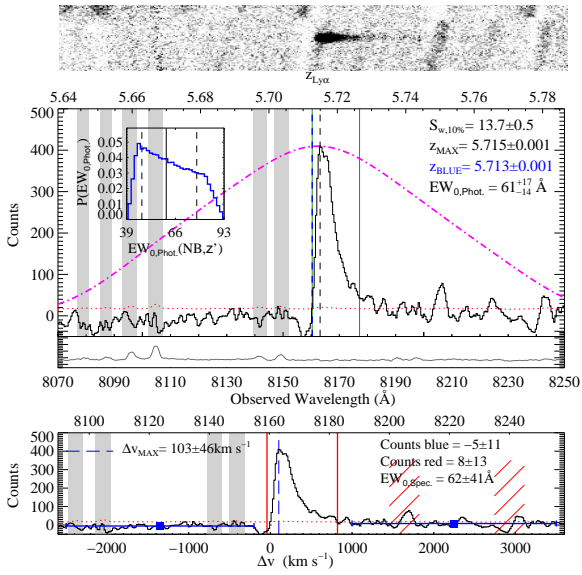


Figure B25. Field J1137+3549. ID 5

LAE 113647.09+354402.2

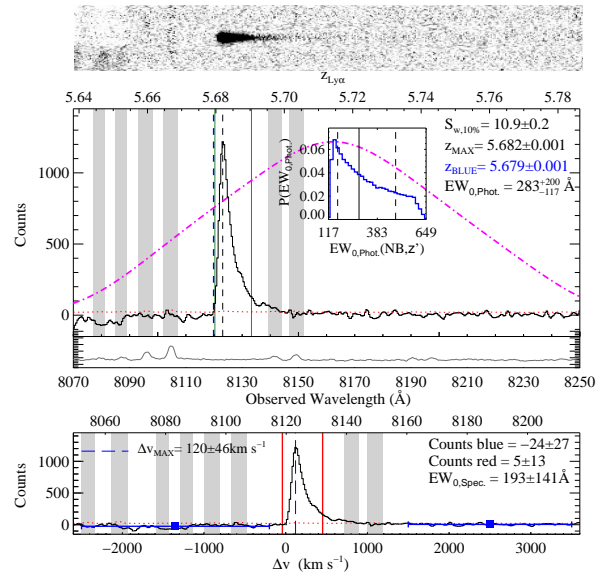


Figure B27. Field J1137+3549. ID 7

LAE 113718.6+355300.4

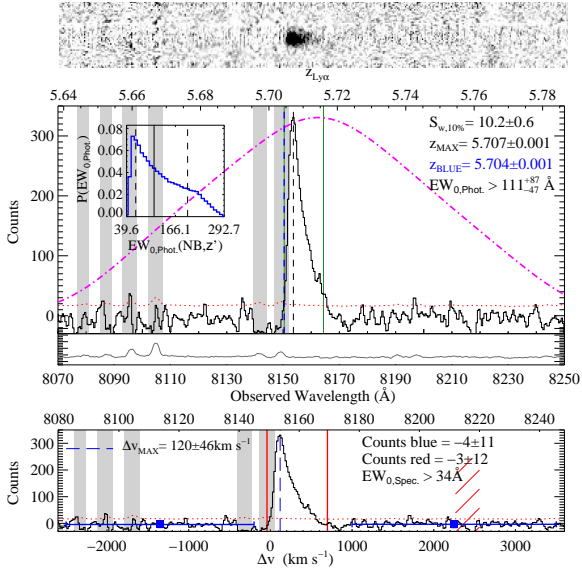


Figure B28. Field J1137+3549. ID 8

LAE 113701.31+354917.4

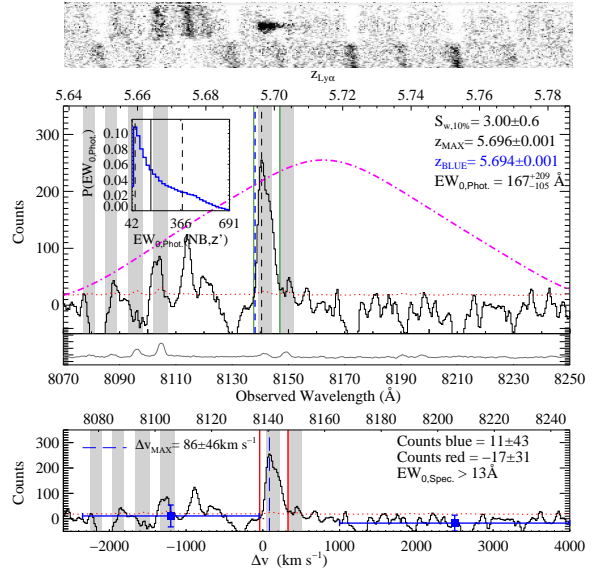


Figure B30. Field J1137+3549. ID 10

LAE 113805.27+355811.5 (600ZD)

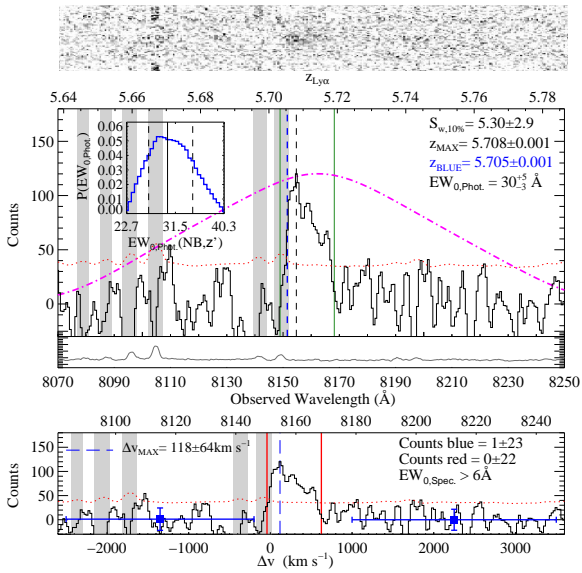


Figure B29. Field J1137+3549. ID 9

LAE 113739.82+355238.2 (600ZD)

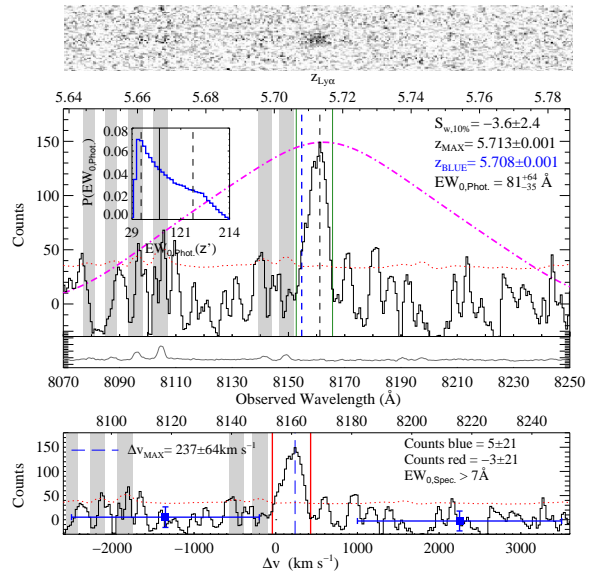


Figure B31. Field J1137+3549. ID 12